Aerodynamic Design Optimization Using the Drag Decomposition Method

François Bisson

Masters of Engineering

Department of Mechanical Engineering

McGill University

Montreal,Quebec

2015-08-11

A thesis submitted to McGill University in partial fulfilment of the requirements for the degree of Masters of Engineering

DEDICATION

This document is dedicated to my grand-fathers: Gérard Bisson and Gérard Turcotte.

ACKNOWLEDGEMENTS

Foremost, I would like to express my deepest gratitude to my advisor, Prof. Siva Nadarajah, for giving me the great opportunity to study under his guidance. His support, patience, and encouragements have made my time at McGill Computational Aerodynamics Group an enriching academic and life experience and I am truly thankful for it.

I am grateful to all my colleague at McGill Computational Aerodynamics Group for their help and fraternity; most particularly, Brian Vermeire, Jean-Sébastien Cagnone, Benjamin Walther, Peyman Khayatzadeh, Philip Caplan, Arthur Dubois-Thaine, Jeremy Schembri, Pierre-Olivier Tardif, Emmett Padway, and Doug Shi-Dong.

I must also thank the National Sciences and Engineering Research Council (NSERC), Le Fond de recherche du Québec - Nature et Technologie, and the Department of Mechanical Engineering of McGill University for their financial support.

Finally, I would like to thank my family, and most particularly my mother and father; without they support, love, and encouragements and the values they have transmitted to me, I would not be the person I am today.

ABSTRACT

The current work applies various drag decomposition methods in an adjoint-based aerodynamic shape optimization framework. In this thesis, the numerical solver based on the Reynolds-averaged Navier-Stokes (RANS) equations is briefly described. The drag decomposition methods, including a novel correction to the induced drag based on an objective vortex sensor, are presented and applied for the drag breakdown in inviscid and viscous flows. The adjoint-based optimization framework is described; particularly, the adjoint principle, the Radial Basis Function (RBF) mesh deformation scheme, and the optimization strategy. Special emphasis is also put on the implementation of the various decomposed drag components. Finally, the proposed approach is applied for the unconstrained and constrained drag minimization of several geometries, namely the DPW-W1 wing, the CRM isolated wing, and a pair of NACA 0012 profile wings, in subsonic-transonic inviscid and viscous flows.

ABRÉGÉ

Ce travail applique plusieurs méthodes de décomposition de traînée à l'intérieur d'un système basé sur la méthode adjointe pour l'optimization aérodynamique de géométrie. Dans cette thèse, le solveur numérique basé sur les équations moyennes de Navier-Stokes (RANS) est brièvement présenté. Les méthodes de décomposition de traînée, incluant une nouvelle correction de traînée induite se basant sur un détecteur de vortex, sont présentées et appliquées à des écoulements visqueux et non-visqueux. Le système d'optimization à méthode adjointe est aussi décrit; plus particulièrement le principle adjoint, la méthode de déformation de maillage à fonctions basiques radiale(RBF) et la stratégie d'optimization. Une emphase spéciale est donnée à l'implémentation des plusieurs composantes de traînée. Finalement, l'approche proposée est appliquée pour la reduction de traînée non-constrainte et contrainte pour quelques géométries à l'intérieur d'écoulement visqueux et non-visqueux.

TABLE OF CONTENTS

LIST OF TABLES

LIST OF FIGURES

CHAPTER 1
Introduction

Rising fuel prices and environmental concerns demand multiple strategies to improve fuel efficiency in the aviation industry. To this end, drag prediction and minimization remain important topics in the engineering and aerospace science communities. The advent of Computational Fluid Dynamics (CFD) as a mature and widely accepted analysis tool combined with more robust numerical optimization methods have assisted designers to increase the aerodynamic performance and improve their understanding of the design space.

CFD drag prediction methods can be summarily divided into two approaches: near-field, and far-field. Surface integration of pressure and skin friction, also known as the near-field method, is typically used to predict drag and lift forces from CFD computations. This method only allows distinction between the mechanical components of drag, namely pressure and skin friction drags. However, the far-field drag decomposition methods, described in [41, 15, 37, 44], allow for phenomenological breakdown of the drag components (induced, wave, profile), as well as the estimation of spurious drag. This latter feature reduces the drag prediction dependency on mesh resolution when compared to the near-field approach.

The series of CFD Drag Prediction Workshops [5] held by The American Institute of Aeronautics and Astronautics (AIAA) serves as a forum where academic and industry leaders compare tools for aircraft force and moment prediction. The last

workshop, the 5th [2], was held on June 2012 and had over 22 participating teams or organizations. The geometry studied in the workshop is the Common Research Model (CRM) which is representative of a modern transonic commercial transport airplane [3]. Comparison of the participants' continuum near-field drag estimates shows a standard deviation of 5.3 drag counts at the finest grid level, which corresponds to $\sim 2\%$ of the total drag (1 drag count corresponds to $C_D = 0.0001$) [29]. This large discrepancy further emphasises the difficulty of the aerospace community to measure drag accurately using CFD. Furthermore, at the medium grid level, total drag values are scattered by more than 25 drag counts (i.e. $\sim 10\%$ of total drag); where the medium grid level represents a typical grid size used for design studies. Employing the far-field drag decomposition approach, Ueno et al. [41] and Hue et al. [21] demonstrated that spurious drag can account for 9 drag counts at the coarser grid level, and 4 drag counts at the medium grid level. Hence the large sensitivity to grid size and quality raises concerns on the application of CFD for aircraft design.

Aerodynamic shape optimizations are often performed using the near-field drag prediction method on coarse to medium meshes due to the need to simulate a large number of cases for trade-studies. The presences of a significant amount of spurious drag may pollute the optimization process by influencing the design towards an artificial optimum. In fact, Yamazaki et al. [46] demonstrated through the use of the drag decomposition that final optimum aircraft shapes were influenced by the presence of spurious drag within an aerodynamic design optimization study.

Therefore, an optimization process strictly based on the physical components of drag would remove the influence of the spurious drag contribution, thus, reducing mesh dependency. More meaningful designs could potentially be obtained at a substantially lower computational expense. Furthermore, the efficiency of the aerodynamic shape optimization could be enhanced by assigning design variables best suited for each phenomenological component of drag. Such approach could represent an innovative design tool capable of exploring radically new designs, and allowing high-fidelity optimization to be used in earlier phases of the design.

Aerodynamic optimization of drag components has been notably investigated. Recently, Ning et al. [36] used low-fidelity models to perform conceptual studies of non-planar wings. In the study, the induced and profile drags were estimated using the panel method with strip theory in addition to approximations for weight, and stall speed. The author pointed out that the work could be expanded to yield additional insights: such proposed extensions include considerations for high-fidelity modelling of transonic drag rise, and airfoil section design.

Hicken et al. [20] used inviscid CFD for the aerodynamic shape optimization of non-planar wings in subsonic flow. Near-field drag was used to drive the optimization; winglets and box-wing designs were investigated. The conclusions were limited to the inviscid subsonic assumption, and thus did not consider viscous and turbulent effects as well as transonic effects on drag.

Yamazaki et al. [45] used the far-field drag decomposition method and a genetic algorithm to explore tradeoffs between the wave and induced drags for the design of airfoils, planform shape, and winglets. The use of physical components of drag

allowed the author to investigate drag-reduction mechanisms. However, a major drawback of this approach is the large number of computationally costly high-fidelity CFD simulations required by the genetic algorithm to reach an optimum solution.

Therefore in this work, we propose to employ a gradient based method together with the far-field drag decomposition approach for the aerodynamic design of aircraft wings. However, a challenge with gradient-based optimization methods is the high cost associated with the evaluation of the sensitivity of the objective function with respect to the design parameters. For problems where the number of design parameters outweigh the number of objective functions by a large margin, the adjoint approach provides an efficient technique to evaluate gradients at a relatively low cost. A major aspect of the work presented in this thesis relates to the derivation of the gradients (a.k.a. sensitivities) of various far-field drag components using the adjoint approach and their implementation into a gradient-based optimization framework.

The sensitivities of the various drag components obtained through the adjoint-based approach could also be used to deepen the understanding of the impact of various design parameters, such as wing planform and winglet design parameters, on the aerodynamic components of drag. Exhaustive studies on the response of each drag component could be performed, and their sensitivities used by designers to gain insights on the design space.

1.1 Contribution and Thesis Overview

The goal of the current work is to develop and demonstrate gradient-based optimization through the adjoint approach using various decomposed components of drag. The main contributions presented in this thesis are: the definition and validation of a *Q-criterion* based correction to induced drag, and the derivation and implementation of the discrete adjoint solver terms for the far-field drag components in a high-fidelity adjoint-based optimization framework.

The following chapters are structured as follows. Chapter 2 describes the flow governing equations and the various drag decomposition techniques. Chapter 3 presents the adjoint-based optimization framework. Chapter 4 demonstrates drag decomposition validations. Chapter 5 presents optimization results performed with the proposed approach, and finally Chapter 6 summarizes the main conclusions of the thesis and proposes future work.

CHAPTER 2
The Governing Equations and Drag Decomposition

The governing equations and numerical discretization employed in the flow solver are described in the first section of this chapter. In the following section, different drag decomposition techniques are discussed along with their implementation.

2.1 The Governing Equations

The conservative form of the 3D compressible Reynolds-averaged Navier-Stokes equations (RANS) in Cartesian coordinates x_1, x_2, and x_3 are described, using Einstein notation, by

$$\frac{\partial \mathbf{w}}{\partial t} + \frac{\partial \mathbf{f_i}}{\partial x_i} - \frac{\partial \mathbf{f_{v,i}}}{\partial x_i} = 0 \quad \text{in } V, \tag{2.1}$$

where the state vector $\mathbf{w}$, inviscid flux vector $\mathbf{f_i}$ and viscous flux vector $\mathbf{f_{v,i}}$ are defined as,

$$\mathbf{w} = \begin{bmatrix} \rho \\ \rho u_1 \\ \rho u_2 \\ \rho u_3 \\ \rho E \end{bmatrix}, \quad \mathbf{f_i} = \begin{bmatrix} \rho u_i \\ \rho u_i u_1 + p\delta_{i1} \\ \rho u_i u_2 + p\delta_{i2} \\ \rho u_i u_3 + p\delta_{i3} \\ \rho E u_i + p u_i \end{bmatrix}, \quad \mathbf{f_{v,i}} = \begin{bmatrix} 0 \\ \tau_{ij}\delta_{i1} \\ \tau_{ij}\delta_{i2} \\ \tau_{ij}\delta_{i3} \\ u_j \tau_{ij} + k\frac{\delta T}{\delta x_i} \end{bmatrix}.$$

The density, velocities, Kronecker delta function, the total energy, and viscous stresses are respectively denoted as ρ, u_i, δ_{ij}, E, and τ_{ij}. The total energy is given by

$E = e + \frac{1}{2}(u_i u_i)$. The pressure p is determined by the equation of state

$$p = (\gamma - 1)\rho \left[E - \frac{1}{2}(u_i u_i) \right],$$

where γ is the ratio of specific heats. Steady state solutions are considered in this study. For the inviscid solutions presented in this thesis, the viscous fluxes are set to zero assuming adiabatic surfaces, and negligible viscous stresses; the Euler equations are thus solved.

2.1.1 Numerical Discretization

Eq. (2.1) can be represented in semi-discrete form as,

$$\mathcal{V}\frac{\partial \mathbf{w}}{\partial t} + R(\mathbf{w}) = 0 \quad \text{in } \mathcal{D}, \tag{2.2}$$

where $\mathcal{V}$ is the volume, $R(\mathbf{w})$ is the residual comprised of the convective and dissipative fluxes, and $\mathcal{D}$ is the computational domain. The RANS solver used for this study uses a cell-centered finite volume numerical scheme with the Jameson-Schmidt-Turkel (JST) [26] or enthalpy-based convective upwind and split pressure (H-CUSP) [24] dissipation, and a five-stage modified Runge-Kutta with local time-stepping. Turbulent viscosity is computed with either Menter's two equations k-ω shear stress transport (SST) [34] or the Baldwin-Lomax [6] turbulence model. Residual averaging and multigrid techniques are used to accelerate the convergence.

The reader is referred to the work of Nadarajah [35] and Walther [42] for a more thorough description of the numerical discretization.

2.2 Drag Decomposition

This section summarizes the near-field and far-field drag decomposition methods. Alternative formulations of the far-field drag are discussed.

2.2.1 Near-Field Method

Conservation of momentum can be applied on the surface of an aircraft to determine the near-field drag,

$$D = \iint_{\mathrm{S_{body}}} [-pn_x + \tau_{xx}n_x + \tau_{xy}n_y + \tau_{xz}n_z - \rho(u - U_\infty)(\mathbf{u} \cdot \mathbf{n})]dS. \tag{2.3}$$

where $\mathbf{n}$ is the normal vector with components, n_x, n_y, and n_z, τ is the shear stress tensor, p the pressure, and $\mathbf{u}$ is the velocity vector.

The fifth term reduces to zero due to the no-slip boundary condition ($\mathbf{u} \cdot \mathbf{n} = 0$) thus reducing the expression to the integration of pressure and skin friction on the surface of the aircraft only.

$$D_{NF} = \iint_{\mathrm{S_{body}}} [-pn_x + \tau_{xx}n_x + \tau_{xy}n_y + \tau_{xz}n_z]dS, \tag{2.4}$$

The components (pressure and skin friction) from Eq. (2.4) may be physically interpreted as the mechanical components of drag. This approach is typically used for drag prediction and minimization due to its simplicity and ease of implementation.

2.2.2 Far-Field Method

As the near-field approach expresses the forces acting on the solid body by the surrounding fluid, the far-field approach formulates the opposite and equal forces -

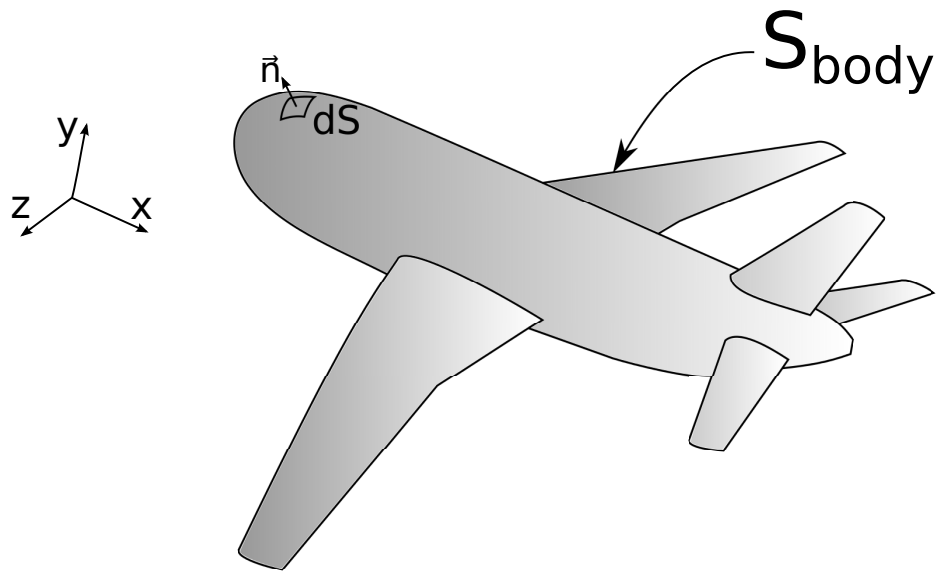

(a) Body Forces

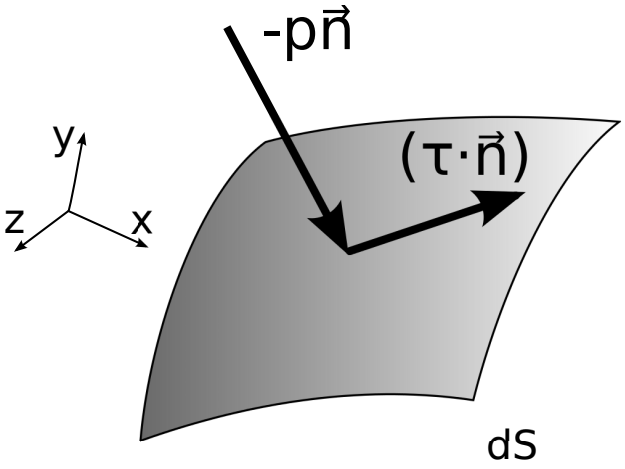

(b) Surface Element

Figure 2–1: Schematic of near-field integration

i.e. the forces acting on the surrounding fluid by the solid body - through Newton's third law.

While there are several variations of the final expression for far-field drag components, they are all based on the conservation of momentum on a closed surface ($S_{\text{ff-ext}}$) surrounding the aircraft,

$$D = \iint_{S_{\text{ff-ext}}} [-pn_x + \tau_{xx}n_x + \tau_{xy}n_y + \tau_{xz}n_z - \rho(u - U_\infty)(\mathbf{u} \cdot \mathbf{n})]dS, \tag{2.5}$$

where $S_{\text{ff-ext}}$ is chosen to be far enough from the aircraft surface, and the viscous stresses are assumed negligible. An arbitrary control volume is depicted on Figure 2–2(a).

A further step is taken to decompose Eq. (2.5) into the various aerodynamic components of drag (induced, wave, and viscous drag), and a spurious drag component introduced by the artificial dissipation associated with the numerical scheme and the grid coarseness,

$$D = D_{\text{induced}} + D_{\text{wave}} + D_{\text{viscous}} + D_{\text{spurious}}.$$

The decomposition is achieved by introducing the notion of thermodynamic *reversible*, and *irreversible* processes. In this section, alternative expressions for these components are briefly presented. The reader is referred to cited publications [15, 16, 28, 33, 37] for more thorough derivations.

Viscous, Wave, and Spurious Drag

From a thermodynamic point of view, the viscous, wave, and spurious drags are associated with *irreversible* processes occurring inside the domain such as shock waves, viscous and artificial dissipation respectively.

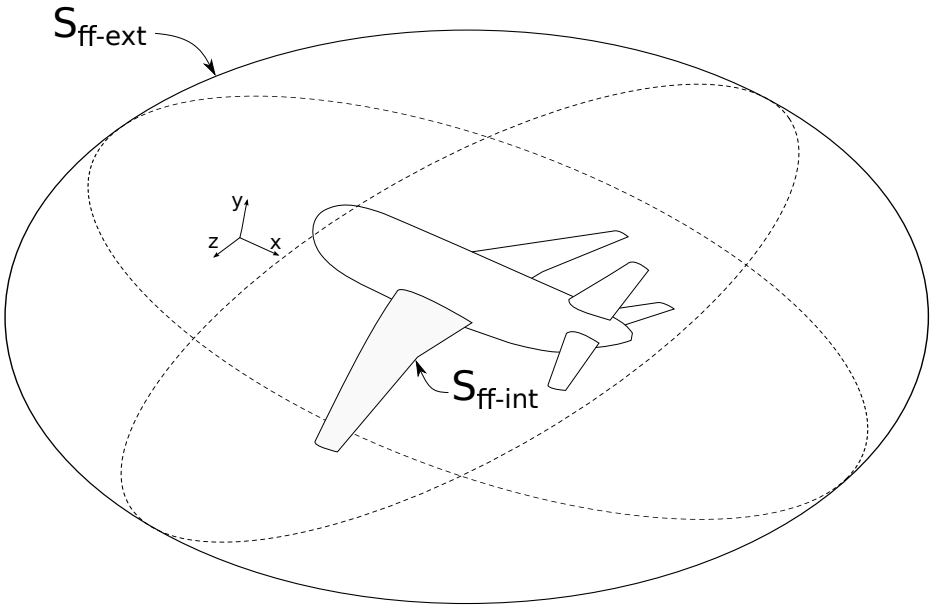

(a) Far-field Surfaces

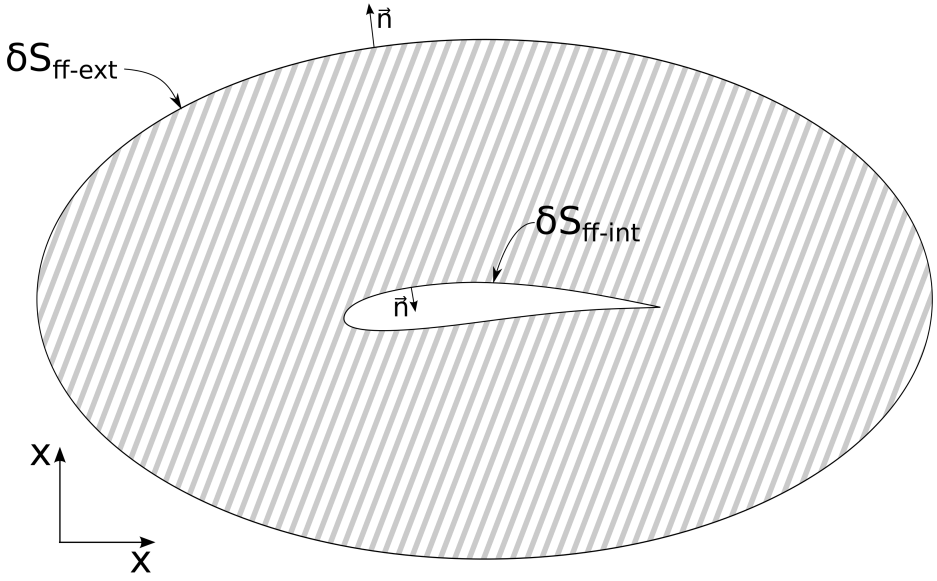

(b) $x - y$ slice

Figure 2–2: Schematic of far-field integration

By reformulating Eq. (2.5) in terms of thermodynamic variables, Destarac [15] expressed the sum of *irreversible* drag components as,

$$D_{\text{wave}} + D_{\text{viscous}} + D_{\text{spurious}} = - \iint\limits_{\text{S}_{\text{ff-ext}}} [\rho \Delta \overline{u} (\mathbf{u} \cdot \mathbf{n})] dS, \tag{2.6}$$

where the *irreversible* momentum deficit, $\Delta \overline{u}$, is defined as,

$$\Delta \overline{u} = U_\infty \left(\sqrt{1 - \frac{2}{(\gamma - 1) M_\infty^2} \left[\left(e^{\frac{\Delta s}{R}} \right)^{\frac{\gamma - 1}{\gamma}} - 1 \right] + \frac{2 \Delta H}{U_\infty^2}} - 1 \right). \tag{2.7}$$

After approximating Eq. (2.6) and considering only the leading order term, or by applying a small perturbation as described by [28, 37] to Eq. (2.5), the sum of the *irreversible* components of drag can be alternatively expressed as net entropy fluxes inside the domain,

$$D_{\text{wave}} + D_{\text{viscous}} + D_{\text{spurious}} = D_{\Delta s} = \frac{1}{\gamma M_\infty^2} \iint\limits_{\text{S}_{\text{ff-ext}}} \left(\frac{\Delta s}{R} \right) \rho (\mathbf{u} \cdot \mathbf{n}) \, dS + \mathcal{O}(\Delta^2). \tag{2.8}$$

To decompose the various *irreversible* components of drag, the surface integration on $\text{S}_{\text{ff-ext}}$ may be transformed into a volume integration through the Gauss's divergent theorem,

$$D_{\text{wave}} + D_{\text{viscous}} + D_{\text{spurious}} = - \iint\limits_{\text{S}_{\text{ff-ext}}} [\rho \Delta \overline{u} (\mathbf{u} \cdot \mathbf{n})] dS = - \iiint\limits_{V} \nabla \cdot \rho \left(\Delta \overline{u} \right) \mathbf{u} \, dV. \tag{2.9}$$

Then, the integral over the volume from Eq. (2.9) can then be sub-divided into regions associated with the various *irreversible* processes. The shock detection

function from Lovely et al. [31] was used to determine the shock region:

$$f_{\text{shock}} = \frac{\mathbf{u} \cdot \nabla p}{a|\nabla p|} \geq 1. \tag{2.10}$$

A sensor based on turbulent viscosity is used to determine the boundary-layer and wake regions, [37]

$$f_{\text{viscous}} = 1 + \frac{\mu_t}{\mu_l} > k_{bl} k_{\text{inf}}, \tag{2.11}$$

where μ_l and μ_t are the laminar and turbulent viscosities respectively. The cutoff constant, k_{bl}, is set to 1.1: such value allows to limit integration to the viscous turbulent region where $\mu_t > \mu_l$. Ueno et al. [41] studied the effects of the cutoff constant on the viscous drag for the CRM case and determined that a cutoff value between 0.1 and 10 was providing equivalent results. The spurious drag is thus estimated by the region of the domain neither associated with shock or viscous regions.

Induced Drag

One approach to express the induced drag is to simply remove the total *irreversible* drag (Eq. (2.6)) from the net momentum balance on $\mathrm{S}_{\text{ff-ext}}$. The induced drag, or total *reversible* drag, is thus obtained,

$$D_i = -\iint_{\mathrm{S}_{\text{ff-ext}}} [\rho(u - U_\infty - \Delta\overline{u})(\mathbf{u} \cdot \mathbf{n}) + (p - p_\infty) n_x] dS, \tag{2.12}$$

where n_x is the x-component of the normal vector $\mathbf{n}$. The x-,y-,and z-components of the velocity vector $\mathbf{u}$ are u, v, and w respectively.

Alternatively, one may consider $\mathrm{S}_{\text{ff-ext}}$ to be defined as shown in Fig. 2–3, where the upstream ($\mathrm{S}_{\text{ff-u}}$) and lateral ($\mathrm{S}_{\text{ff-lat}}$) boundaries are far from the solid body

where $u \to U_\infty$, v & $w \to 0$ and $p \to p_\infty$. Then, by applying small perturbation theory [28], an expression for induced drag that only involves integration on the downstream plane ($S_{\text{ff-d}}$) is obtained,

$$D_i = \frac{\rho_\infty}{2} \iint\limits_{S_{\text{ff-d}}} (v^2 + w^2) dS - \frac{\rho_\infty}{2} \iint\limits_{S_{\text{ff-d}}} (1 - M_\infty^2)(u - U_\infty)^2 dS + \mathcal{O}(\Delta^3). \tag{2.13}$$

Giles et al. [16] extended Maskell's contribution [33] and showed that the integration over the whole crossflow plane can be reduced to an integration over the wake region, claiming to reduce the error introduced by large computational elements away from the wake region,

$$D_i = \frac{\rho_\infty}{2} \iint\limits_{S_{\text{wake}}} (\psi\zeta) dS + \mathcal{O}(\Delta^3), \tag{2.14}$$

where ψ and ζ are respectively the stream function and the x-component of vorticity on the wake plane.

Correction to Induced Drag for Tip Vortex Dissipation

Any large vortex will dissipate downstream by the combined effects of the numerical scheme and coarseness of the grid prior to reaching $S_{\text{ff-ext}}$ causing drag to shift from induced drag to *irreversible* drag. In order to minimize this spurious effect and obtain a more accurate estimation of induced drag, we propose a novel correction based on the net *irreversible* drag produced inside the vortex region by employing

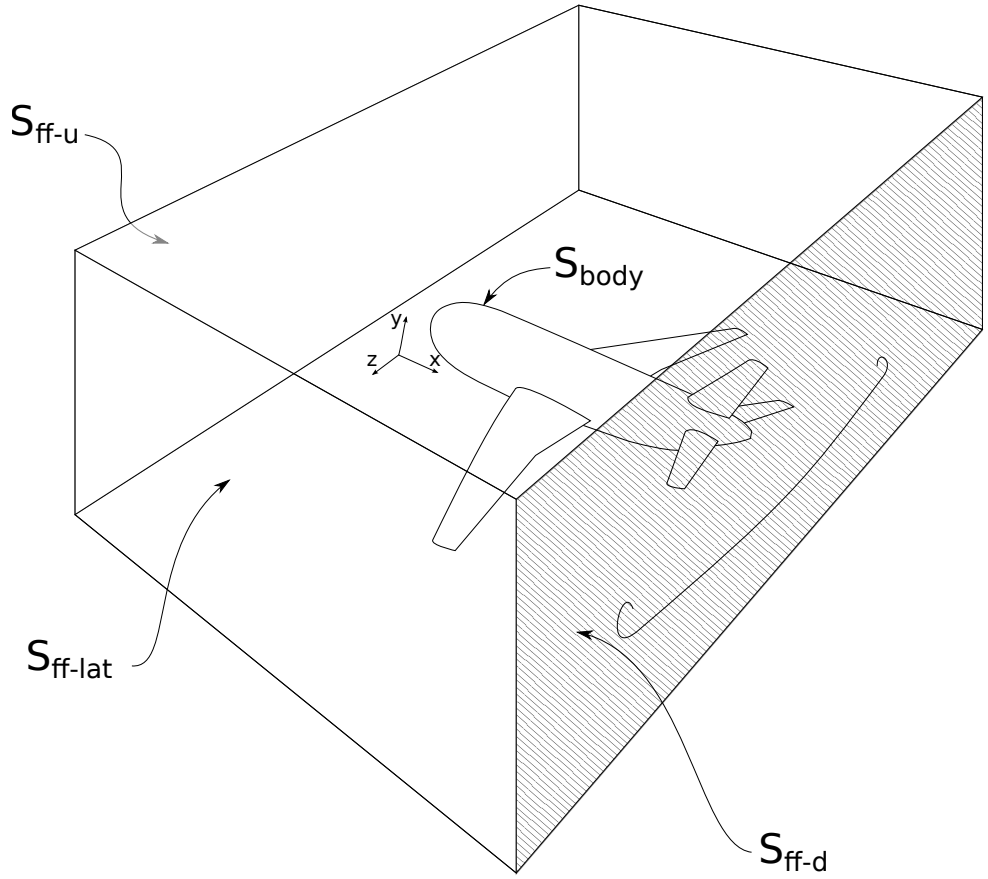

Figure 2–3: Schematic of far-field integration for crossflow plane integration

the Q-criterion [19] to define the tip vortex region.

$$D_{i-Q} = D_i + \Delta D_{i-Q} = D_i - \iint_{\mathrm{S_{vortex}}} [\rho \Delta \overline{u}(\mathbf{u} \cdot \mathbf{n})] dS. \tag{2.15}$$

The surface of integration, $\mathrm{S_{vortex}}$, is obtained through the Q-criterion,

$$Q = \frac{1}{2}\left[|\Omega|^2 - |S|^2\right] > 0, \tag{2.16}$$

where Ω and S are the vorticity and strain tensors, respectively.

Lift

Following a similar methodology than for drag, the lift can be alternatively obtained from a wake plane integration as [28],

$$L_{wake} = \rho_\infty U_\infty \iint_{S_{Wake}} (y\zeta) dS. \tag{2.17}$$

2.2.3 Numerical Implementation

The following various far-field drag components were implemented as a post-processing step in the flow solver:

1. Wave, viscous and spurious drag as per net entropy flux formulation (Eq. (2.9))
2. Wave, viscous and spurious drag as per Destarac's momentum deficit formulation (Eq. (2.6))
3. Induced drag as per total reversible drag formulation (Eq. (2.12))
4. Induced drag as per Maskell's crossflow plane formulation (Eq. (2.14))
5. Induced drag as per total reversible drag formulation with the addition of Q-criterion based correction (Eq. (2.15))

While items 1, 2, 3, and 5 are relatively straightforward to implement - only the net flux of state variables across predetermined mesh elements is required; however the discretization and implementation of Maskell's induced drag (item 4) is more demanding. The latter requires a plane slicing algorithm and a tailored Poisson's equation solver to determine the stream function (ψ) on the crossflow plane (Eq. (2.14)).

The numerical implementation proposed by Giles et al. [16] was used for the results presented in this thesis. This approach requires the interpolation of the

structured grid on the crossflow plane to build a 2D unstructured mesh based on a *marching cube* algorithm [30]. Then, using Green's analytical function, the Maskell's induced drag can be evaluated using the following discrete summation,

$$D_i = \frac{1}{2}\rho_\infty \sum_\alpha \sum_\beta \Gamma_\alpha \Gamma_\beta d_{\alpha,\beta}, \tag{2.18}$$

where,

$$d_{\alpha,\beta} = -\frac{1}{12\pi}\sum_j \log[(y_j - y_\beta)^2 + (z_j - z_\beta)^2] - \log[(y_j - y_\beta)^2 + (z_j + z_\beta)^2]. \tag{2.19}$$

The α and β loops in Eq. (2.18) denote looping over the triangular cell element centroid. The j summation of Eq. (2.19) is performed over the three nodes of the triangular cell α. The circulation Γ_i around a triangular mesh element is defined as,

$$\Gamma_i = \sum_{edges} (\overline{v}^* \Delta y + \overline{w}^* \Delta z) = \sum_{j=1}^{3} (\overline{v}^* \Delta y + \overline{w}^* \Delta z)_j, \tag{2.20}$$

where $\overline{v}^*$ and $\overline{w}^*$ are the average velocity components on the edge of a cell element. The superscript * denotes the crossflow velocity components defined as,

$$\begin{aligned} v^* &= v\cos\alpha - u\sin\alpha, \\ w^* &= w, \end{aligned}$$

where u, v, w are the velocity components. The discrete expression for circulation described in Eq. (2.20) echoes the Green's theorem stating that the area integral of the vorticity is equal to the circulation around the boundary of an arbitrary area C,

i.e.

$$\iint_C \zeta dA = \oint_{\partial C} \mathbf{u} \cdot \mathbf{dS}. \tag{2.21}$$

CHAPTER 3
Optimization Framework

This chapter discusses the adjoint approach, the mesh movement scheme, and the optimization strategy. These components contribute to the optimization framework used for the results presented in later chapters.

3.1 Sensitivity Analysis via the Adjoint Approach

The adjoint approach, introduced by Pironneau [39] to study elliptical partial differential equations and extended to transonic flow by Jameson [25], procures the gradient of any objective function independently of the number of design variables by solving the adjoint system. A gradient-based optimization based on this approach is thus more efficient when compared to methods relying on more classical means of computing those sensitivities (i.e. finite-difference and complex step). The gain is particularly sensible when high-fidelity models are used. Designers have explored several combinations of objective functions and constraints to seek for the best aerodynamic efficiency allowed in prescribed design spaces. The following presents details on the derivation of the adjoint based sensitivities.

Consider an objective function, $I(\mathbf{w}, \mathbf{x}_p)$, to be minimized, where $\mathbf{w}$ is the vector of the conservative flow variables, and $\mathbf{x}_p$ are the geometry control points that define the surface. The residual of the flow solver, which is a function of the conservative

flow variables, $\mathbf{w}$, and control points, $\mathbf{x}_p$, equals to zero for a well converged solution,

$$\mathbf{R}(\mathbf{w}, \mathbf{x}_p) = 0. \tag{3.1}$$

The gradient of the objective function, $I(\mathbf{w}, \mathbf{x}_p)$, with respect to the control points, $\mathbf{x}_p$, is obtained by defining the Lagrangian function

$$L(\mathbf{w}, \mathbf{x}_p, \boldsymbol{\psi}) = I(\mathbf{w}, \mathbf{x}_p) + \boldsymbol{\psi}^T \mathbf{R}(\mathbf{w}, \mathbf{x}_p). \tag{3.2}$$

The sensitivity of the Lagrangian function with respect to the design variable vector can be expanded as,

$$\frac{dL}{d\mathbf{x}_p} = \frac{\partial I}{\partial \mathbf{w}} \frac{d\mathbf{w}}{d\mathbf{x}_p} + \frac{\partial I}{\partial \mathbf{x}_s} \frac{d\mathbf{x}_s}{d\mathbf{x}_p} + \boldsymbol{\psi}^T \left[\frac{\partial \mathbf{R}}{\partial \mathbf{w}} \frac{d\mathbf{w}}{d\mathbf{x}_p} + \frac{\partial \mathbf{R}}{\partial \mathbf{x}_v} \frac{d\mathbf{x}_v}{d\mathbf{x}_p} \right],$$

where the volume mesh points, $\mathbf{x}_v(\mathbf{x}_s(\mathbf{x}_p))$, and the surface mesh points, $\mathbf{x}_s$, are functions of the geometry control points, $\mathbf{x}_p$. To eliminate the flow variable sensitivities, we may, 1^{st} rewrite the expression as

$$\frac{dL}{d\mathbf{x}_p} = \left[\frac{\partial I}{\partial \mathbf{w}} + \boldsymbol{\psi}^T \frac{\partial \mathbf{R}}{\partial \mathbf{w}} \right] \frac{d\mathbf{w}}{d\mathbf{x}_p} + \left[\frac{\partial I}{\partial \mathbf{x}_s} + \boldsymbol{\psi}^T \frac{\partial \mathbf{R}}{\partial \mathbf{x}_v} \frac{d\mathbf{x}_v}{d\mathbf{x}_s} \right] \frac{d\mathbf{x}_s}{d\mathbf{x}_p}, \tag{3.3}$$

where $\frac{d\mathbf{x}_v}{d\mathbf{x}_s}$ is the mesh sensitivity. Finally, one may solve for the Lagrange multipliers ($\boldsymbol{\psi}^T$) such that the first term of the right hand side of Eq. (3.3) is zero,

$$\left[\frac{\partial I}{\partial \mathbf{w}} + \boldsymbol{\psi}^T \frac{\partial \mathbf{R}}{\partial \mathbf{w}} \right] = \mathbf{0}. \tag{3.4}$$

The adjoint system of equations (Eq. (3.4)) are derived by hand and solved with the same five-stage modified Runge-Kutta scheme as that employed for the flow solver. The discrete adjoint approach is used [35] for the results hereby presented. The

gradient expression finally simplifies to

$$\frac{dL}{d\mathbf{x}_p} = \left[\frac{\partial I}{\partial \mathbf{x}_s} + \boldsymbol{\psi}^T \frac{\partial \mathbf{R}}{\partial \mathbf{x}_v}\frac{d\mathbf{x}_v}{d\mathbf{x}_s}\right]\frac{d\mathbf{x}_s}{d\mathbf{x}_p}. \tag{3.5}$$

The final formulation of the gradient shown in Eq. (3.5) thus only depends on the adjoint solution (i.e. the Lagrange multipliers $\boldsymbol{\psi}^T$), the sensitivity of the residual with respect to the volume mesh points($\frac{\partial \mathbf{R}}{\partial \mathbf{x}_v}$), the mesh sensitivities ($\frac{d\mathbf{x}_v}{d\mathbf{x}_s}$), and the parametrization sensitivities ($\frac{d\mathbf{x}_s}{d\mathbf{x}_p}$). The latter three sensitivities are relatively cheap to obtain as they are typically determined either analytically or through an automatic-differentiation procedure. Therefore, the only significantly costly term to evaluate is the adjoint solution which cost is comparable to a flow solution.

An important feature of the adjoint approach is that the cost of gradient evaluation is practically independent of the number of design variables. This is a considerable advantage over finite-difference or complex step approaches for which cost is proportional to the number of design variables.

3.2 Radial Basis Functions (RBFs) Mesh Mover

A meaningful optimization calls for an efficient and robust mesh deformation scheme to ensure mesh quality is maintained during the optimization process. In this study, a mesh deformation scheme based on Radial Basis Functions (RBFs) is employed. This scheme has demonstrated large deformations while maintaining grid orthogonality at the surface [40]. Figure 3–1 shows RBF points on the surface mesh of the Common Research Model (CRM) geometry defined by the Fourth AIAA Drag Prediction Workshop [3]. Figure 3–2 shows ensuing planform deformation to the initial grid.

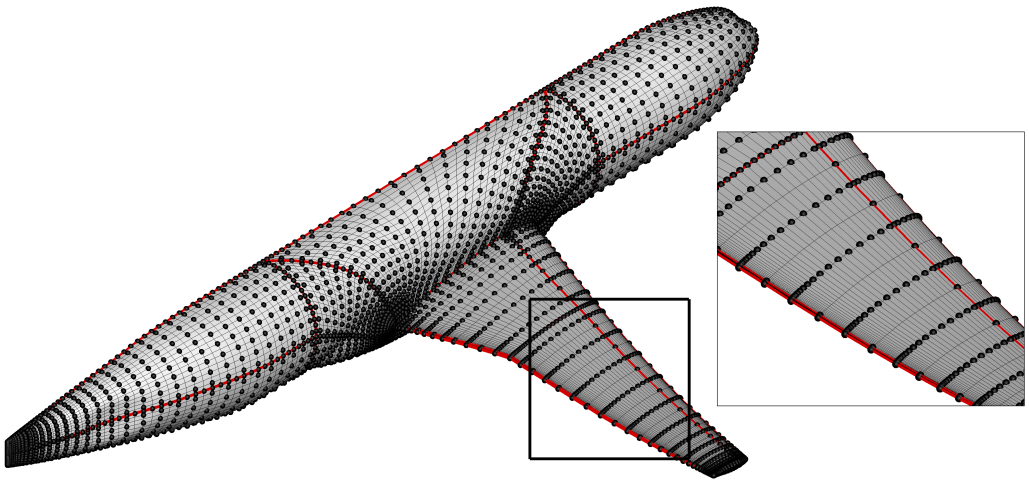

Figure 3–1: RBF points on baseline CRM geometry for a structured grid

RBFs are used in many applications to interpolate scattered data. They can be used in statistics, fluid-structure interactions, neural networks, and in this case mesh deformation. General theory of RBFs can be found in the books *Radial basis functions* [11] and *Scattered data approximation* [43].

The displacement of a volume mesh point located at $\mathbf{x}$ using the RBF interpolating function is defined as,

$$s(\mathbf{x}) = \sum_{i=1}^{N_{rp}} \alpha_i \phi(||\mathbf{x} - \mathbf{x}_{r_i}||), \tag{3.6}$$

where N_{rp} is the number of RBF points, α_i are coefficients, and $||\mathbf{x} - \mathbf{x}_{r_i}||$ is the Euclidean distance between point, $\mathbf{x}$, and the RBF point, $\mathbf{x}_{r_i}$. The coefficients are solved to satisfy the condition that the interpolating function recovers the known displacement at the RBF points $\mathbf{x}_{r_i}$. The basis function used in this study corresponds to Wendland's C^2 [14].

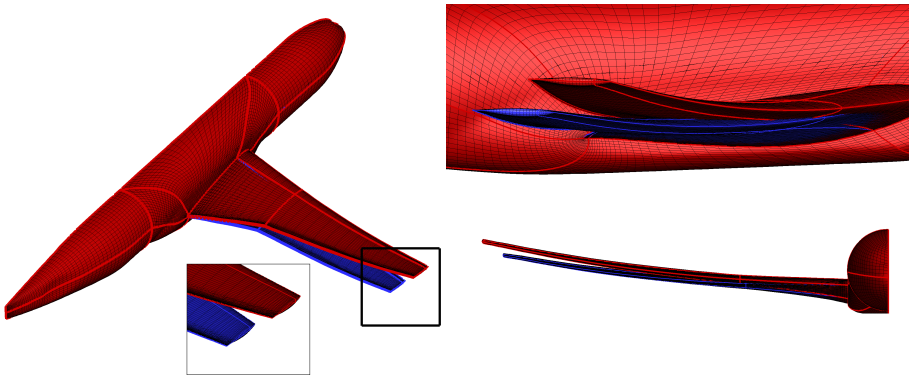

(a) Initial and deformed geometry

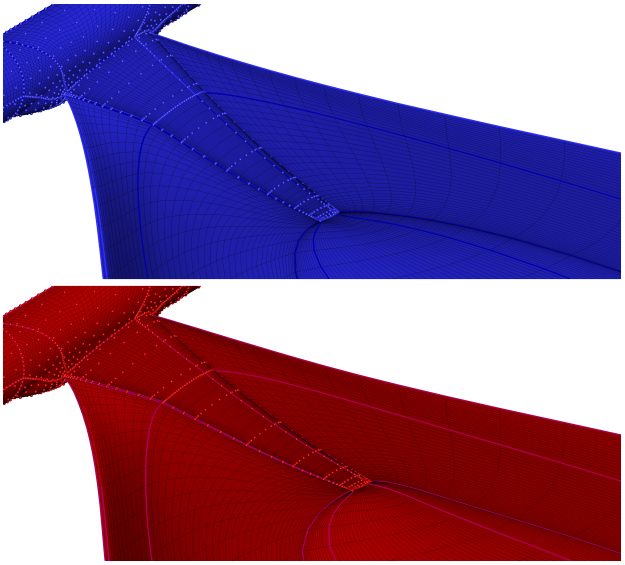

(b) Sample mesh

Figure 3–2: Example of planform deformation for CRM geometry: initial (blue) and deformed (red)

Eq. (3.6), can be conveniently expressed as matrices when considering the entire set of mesh points. First, the coefficients, α_i from Eq. (3.6), must be solved for x, y and z coordinates such that the known displacements at the RBF points, $\Delta\mathbf{x}_r$, are

recovered

$$\Delta \mathbf{x}_r = \mathbf{M}\boldsymbol{\alpha}, \tag{3.7}$$

and the displacements of the volume mesh points $\Delta \mathbf{x}_v$ can then be expressed as

$$\Delta \mathbf{x}_v = \mathbf{A}\boldsymbol{\alpha} = \mathbf{A}\mathbf{M}^{-1}\Delta \mathbf{x}_r, \tag{3.8}$$

where $\mathbf{M} = \begin{pmatrix} \phi_{r_1 r_1} & \phi_{r_1 r_2} & \cdots \\ \phi_{r_2 r_1} & & \\ \vdots & & \ddots \end{pmatrix}_{N_{rp} \times N_{rp}}$, $\mathbf{A} = \begin{pmatrix} \phi_{v_1 r_1} & \phi_{v_1 r_2} & \cdots \\ \phi_{v_2 r_1} & & \\ \vdots & & \ddots \end{pmatrix}_{N_{vp} \times N_{rp}}$, and

$\phi_{v_i r_j}$ represents $\phi(||\mathbf{x}_{v_i} - \mathbf{x}_{r_j}||/SR)$, the basis function between volume point v_i and RBF point r_j, N_{vp} is the number of volume points, SR is the support radius, and $\Delta \mathbf{x}_r$ is the vector of RBF point displacements. An RBF interpolating function must be solved for every coordinate direction, x, y, and z.

The final gradient expression as presented in Eq. (3.5), requires the mesh sensitivity term, $\frac{d\mathbf{x}_v}{d\mathbf{x}_s}$. For the RBF mesh deformation scheme employed; Eq. (3.5) can be expanded to,

$$\frac{dL}{d\mathbf{x}_p} = \left[\frac{\partial I}{\partial \mathbf{x}_s} + \boldsymbol{\psi}^T \frac{\partial R}{\partial \mathbf{x}_v} \frac{d\mathbf{x}_v}{d\mathbf{x}_r} \frac{d\mathbf{x}_r}{d\mathbf{x}_s} \right] \frac{d\mathbf{x}_s}{d\mathbf{x}_p}. \tag{3.9}$$

In the above equation, $\frac{d\mathbf{x}_v}{d\mathbf{x}_r}$ represents the RBF mesh sensitivity, while $\frac{d\mathbf{x}_r}{d\mathbf{x}_s}$ is a $N_{rp} \times N_s$ matrix that maps the designated RBF surface mesh points to all grid points on the surface. In block form it can be represented as

$$\frac{d\mathbf{x}_r}{d\mathbf{x}_s} = \begin{bmatrix} I_{N_{rp}} \\ 0 \end{bmatrix}, \tag{3.10}$$

where $I_{N_{rp}}$ is an identity matrix of size N_{rp}. Lastly, $\frac{d\mathbf{x}_s}{d\mathbf{x}_p}$ is the sensitivity of the surface grid points to each control point and is a vector of length, N_s.

The mesh sensitivities can be derived from Eq. (3.8). Then, the gradient of Eq. (3.9) is simply expressed in each coordinate direction as,

$$\frac{dL}{d\mathbf{x}_p} = \left[\frac{\partial I}{\partial \mathbf{x}_s} - \boldsymbol{\psi}^T \frac{\partial \mathbf{R}}{\partial \mathbf{x}_v} \mathbf{A}\mathbf{M}^{-1} \frac{d\mathbf{x}_r}{d\mathbf{x}_s}\right] \frac{d\mathbf{x}_s}{d\mathbf{x}_p}, \tag{3.11}$$

$$\frac{dL}{d\mathbf{y}_p} = \left[\frac{\partial I}{\partial \mathbf{y}_s} - \boldsymbol{\psi}^T \frac{\partial \mathbf{R}}{\partial \mathbf{y}_v} \mathbf{A}\mathbf{M}^{-1} \frac{d\mathbf{x}_r}{d\mathbf{x}_s}\right] \frac{d\mathbf{y}_s}{d\mathbf{y}_p}, \tag{3.12}$$

$$\frac{dL}{d\mathbf{z}_p} = \left[\frac{\partial I}{\partial \mathbf{z}_s} - \boldsymbol{\psi}^T \frac{\partial \mathbf{R}}{\partial \mathbf{z}_v} \widetilde{\mathbf{A}}\mathbf{M}^{-1} \frac{d\Delta\widetilde{\mathbf{z}}_r}{d\Delta\mathbf{z}_r} \frac{d\mathbf{x}_r}{d\mathbf{x}_s}\right] \frac{d\mathbf{z}_s}{d\mathbf{z}_p}, \tag{3.13}$$

where the term $\dfrac{d\Delta\widetilde{\mathbf{z}}_r}{d\Delta\mathbf{z}_r}$ is due to a scaling in the spanwise z-direction to constraint the points along the symmetry-plane. The reader is referred to Walther [42] for a more thorough description on RBF mesh deformation and its implementation within the structured multiblock flow solver and adjoint based framework used in this thesis.

3.2.1 Application to the Aerodynamic Components of Drag

The derivation of the discrete adjoint source terms and gradient contributions associated with the different components of drag were derived and implemented to the adjoint and gradient computation following the methodology of Nadarajah [35]. To this end, the derivatives with respect to discrete flow state variables, and the discrete mesh points are evaluated for the discrete form of each drag components presented in Chapter 2.2, and implemented into the discrete adjoint solver.

3.3 Optimization Strategies

The following general optimization problem may be considered,

$$\begin{aligned} \min \quad & I(\mathbf{x}_\alpha) \text{ w.r.t. } \mathbf{x}_\alpha \in \Re^n && (3.14) \\ \text{subject to} \quad & c_j(\mathbf{x}_\alpha) = 0, j = 1, ..., m_1 && (3.15) \\ & \widehat{c}_j(\mathbf{x}_\alpha) \geq 0, j = 1, ..., m_2, && (3.16) \end{aligned}$$

where I is the objective function, $\mathbf{x}_\alpha$ the design variables, c_j the equality constraints, and $\widehat{c}_j$ the inequality constraints. A sequential-quadratic programming (SQP) optimization framework is employed to solve the optimization problems presented in this thesis. A considerable advantage of such framework is that, by introducing a Lagrangian function ($L(\mathbf{x}_\alpha, \lambda) = I(\mathbf{x}_\alpha) - \lambda^T c(\mathbf{x}_\alpha)$), the constraints can be directly included into the design problem. Taking the derivatives of the Lagrangian function, the first-order Karush-Kuhn-Tucker (KKT) conditions can be expressed as,

$$F_L(\mathbf{x}_\alpha, \lambda) = \begin{pmatrix} \frac{\partial L}{\partial \mathbf{x}_\alpha} \\ \frac{\partial L}{\partial \lambda} \end{pmatrix} = \begin{pmatrix} \nabla I(\mathbf{x}_\alpha) - \mathbf{A}(\mathbf{x}_\alpha)^T \lambda \\ c(\mathbf{x}_\alpha) \end{pmatrix} = 0, \tag{3.17}$$

where $\mathbf{A}(\mathbf{x}_\alpha)^T = \nabla c(\mathbf{x}_\alpha)$. The SQP framework described in Gill et al. [17] is used to solve the first-order KKT conditions. The search direction and step length are respectively determined through a quasi-newton Broyden-Fletcher-Goldfarb-Shanno (BFGS) method and a general linesearch technique. The SNOPT [18] software package has been employed.

CHAPTER 4
Drag Decomposition Validation

This chapter presents the application of the various drag decomposition alternatives presented in Chapter 2. Mesh refinement studies are performed on different geometries at various flow conditions; the drag decomposition alternatives are compared and discussed.

4.1 DPW-W1 Wing

In this section, the implementations of Kusunose's *irreversible* drag components (Eq. (2.8)) and Maskell's inviscid drag formulation (Eq. (2.14)) are used and compared to drag calculations using the near-field method. The influence of key parameters of the drag decomposition (shock margin, and wake plane location) is first studied. Then, drag polars of the DPW-W1 isolated wing configuration are presented to investigate the validity of the drag decomposition techniques. Aerodynamic shape optimization will be performed on the same geometry in Section 5.2.

A set of three structured C-grid's were used: coarse ($192 \times 32 \times 32$), medium ($192 \times 48 \times 48$), and fine ($256 \times 48 \times 64$). The DPW-W1, a test case from the Third AIAA Drag Prediction Workshop [4], is available in the public domain. Reference quantities are $S_{ref} = 290.322\text{mm}^2$, $C_{ref} = 197.556\text{mm}^2$, $X_{ref} = 154.245\text{mm}^2$ and semispan $b/2 = 762.0\text{mm}$. The flow conditions proposed by the workshop are at a Mach of 0.76 ($M = 0.76$) and lift coefficient of 0.500 ($C_L = 0.500$).

In Figure 4–1, the coefficient of pressure on the upper surface along with the associated shock region volume (V_{shock}) obtained from Eq. (2.10) are presented for the fine grid. As expected, the shock region volume follows closely the strong shock observed at the upper surface of the wing.

Figure 4–2 depicts a sample residual convergence of the flow solver; convergence level approaching machine accuracy (10^{-16}) is obtained. A similar level of convergence is obtained for all conditions studied in this section.

4.1.1 Shock margin

While the shock detection function effectively locates shocks in the domain, it does not always capture all the entropy generated by the shock itself as well as all of the variations, or oscillations, in the CFD solution at the shock vicinity inherent in the flow solver. An extension of the original shock region, obtained where $f_{shock} \geq 1$, is studied in this section.

The strategy employed consists of extending the shock region in the streamwise and vertical directions at the boundaries by a certain number of cells, denoted as the shock margin. A similar strategy is presented in Ueno et al. [41]. Figure 4–3 shows the wave drag for shock margin varying from 0 (the original shock region) to 12 for the three levels of grid at $C_L = 0.500$ and $M = 0.76$.

The wave drag initially drops and stabilizes around 8 drag counts (1 drag count $C_D = 0.0001$) when a shock margin of 6 is reached. Results presented in the next sections are for a shock margin of 8 to allow for some additional extent in the case where stronger shocks might be present.

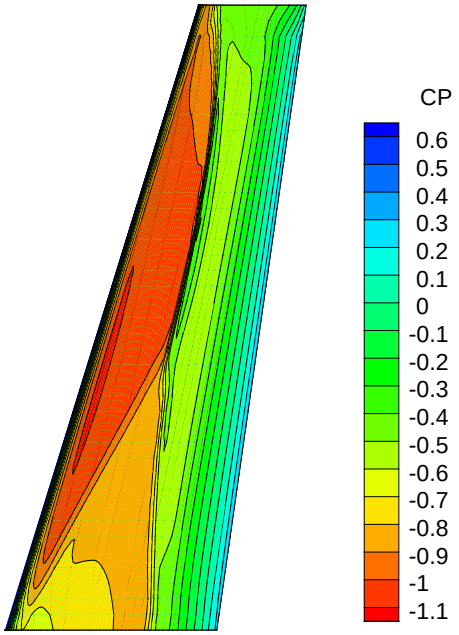

(a) Pressure distribution

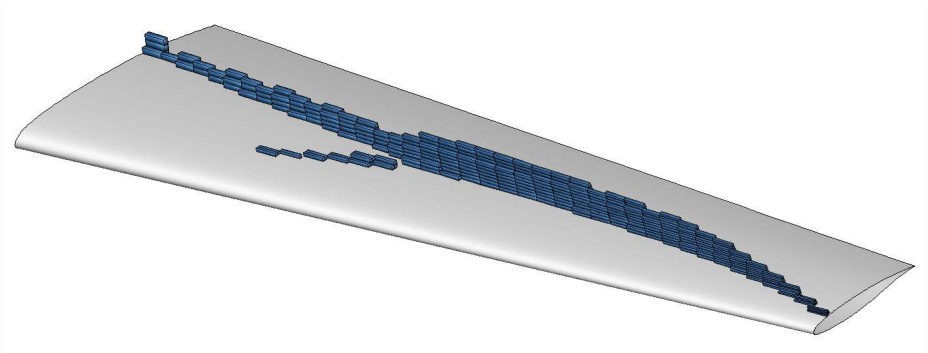

(b) Shock region (V_{shock} for $f_{shock} \geq 1$)

Figure 4–1: DPW-W1 at $M = 0.76$ and $C_L = 0.500$ for fine grid

4.1.2 Location of the wake survey plane

The induced drag is computed on a plane located aft of the model and perpendicular to the freestream flow direction. To be physically consistent, the downstream

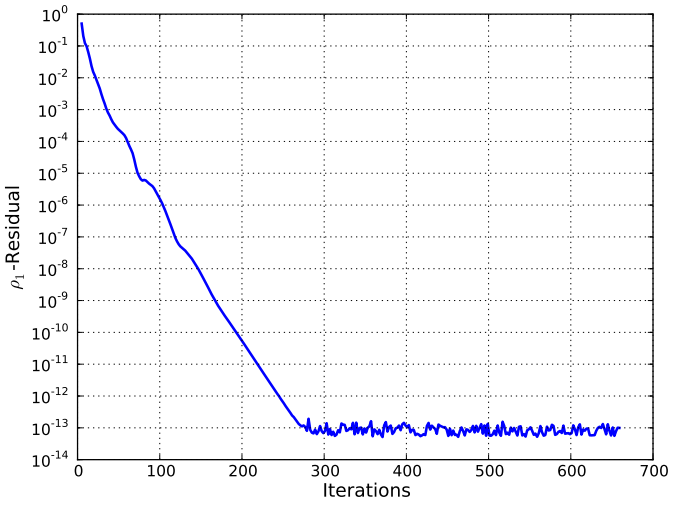

Figure 4–2: DPW-W1 at $M = 0.76$ and $C_L = 0.500$: Residual convergence of flow solver for medium grid ($||R_\rho||_1$ depicted)

boundary of the volume integration must be comprised of the same wake survey plane. As the wake survey plane is moved aft, a shift from induced drag to entropy drag is typically observed as trailing vortices dissipate downstream due to numerical diffusion [13, 22, 41]. Figure 4–4 shows the induced drag ($C_{D_{i-w}}$), entropy drag ($C_{D_{\Delta s}}$), and total drag ($C_{D_{i-w}} + C_{D_{\Delta s}}$) from the far-field drag decomposition as a function of the wake survey location. The plane aft position, x_{wake}, is normalized with the tip chord of the wing, c_{tip}.

For the medium and fine grids, induced drag is consistently shifted to entropy drag up to a wake plane location of $x_{wake}/c_{tip} = 2.5$. This is shown by their sum, the total drag shown on Figure 4–4(b), remaining constant over the interval while induced drag is diminishing by more than 1 drag count. Results for the coarser grid are less consistent; the total drag drops by more than 2 drag counts over the studied

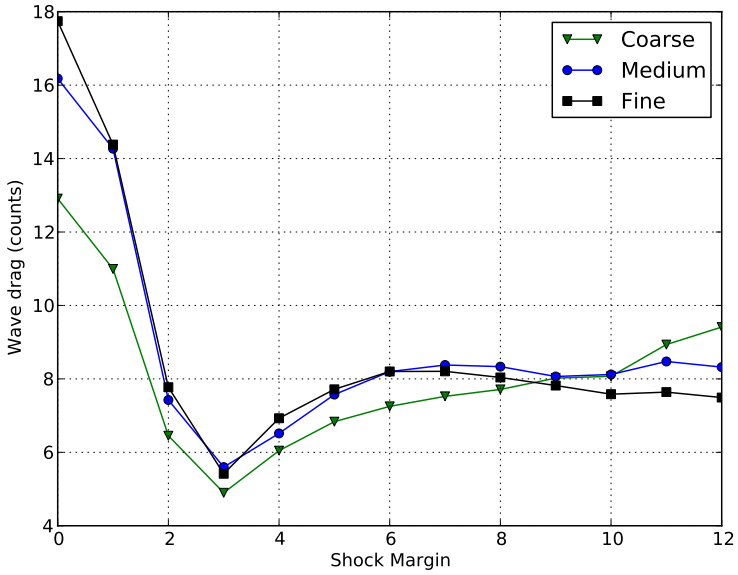

Figure 4–3: DPW-W1 wave drag with respect to shock margin at $M = 0.76$ and $C_L = 0.50$

plane locations. This behaviour may be attributed to the poor resolution of the flow features at the wake obtained with the coarse grid.

Figure 4–4(b) also shows that as the grid is refined, the difference between total drag from the far-field method and the near-field drag (shown with the dotted lines) is reduced; the fine grid showing a total drag difference of less than a drag count over the studied range of wake plane locations. The fine grid allows the flow features to be more accurately resolved downstream, thus allowing valid drag measurements at farther wake plane locations. A wake survey plane location corresponding to $x_{wake}/c_{tip} = 2$ is employed in the later sections.

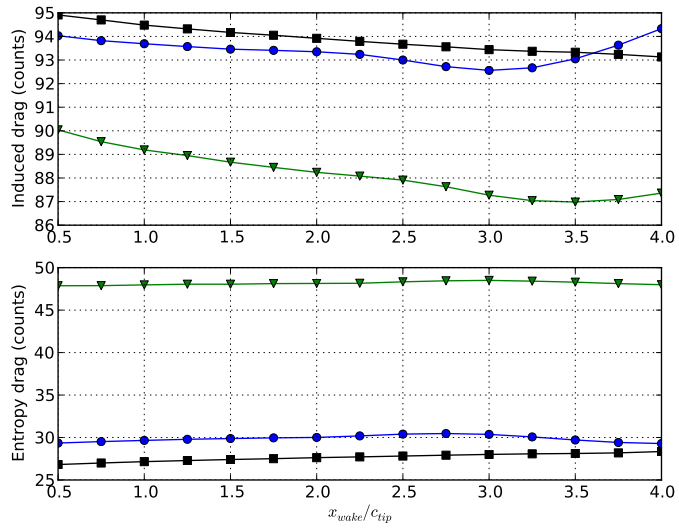

(a) Far-field drag components

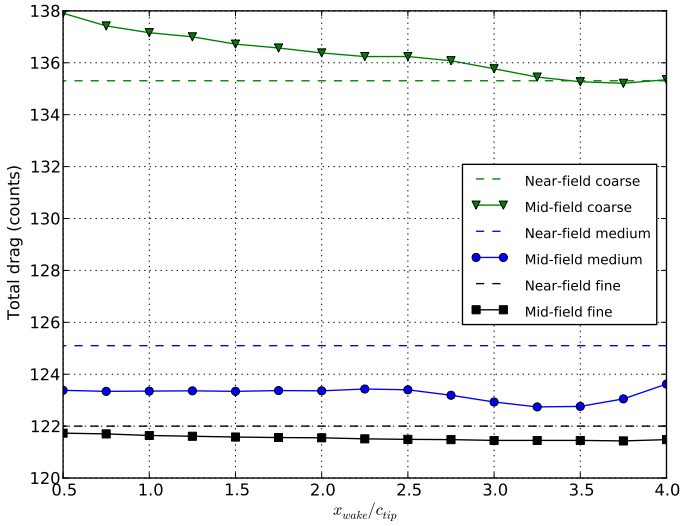

(b) Far-field total drag

Figure 4–4: DPW-W1 drag components versus wake survey plane station

4.1.3 Drag polars

In Figure 4–5(a), the results from the far-field drag decomposition method are shown along with total drag from the near-field method. A good agreement between the wave and induced drags for the coarse, medium, and fine grids is observed. Wave drag differs by less than 1 drag count over the grids studied. The induced drag only differs by $\sim$3 counts between the coarse and the fine grid level; the maximum difference is observed at the largest lift coefficient. The spurious drag reduces with mesh resolution.

As highlighted in Figure 4–5(b), a difference of up to 15 drag counts between the fine and coarse meshes is observed for the near-field method. The far-field approach is much less mesh dependent as the sum of the physical drag components (wave+induced) only shows a difference of 3 counts.

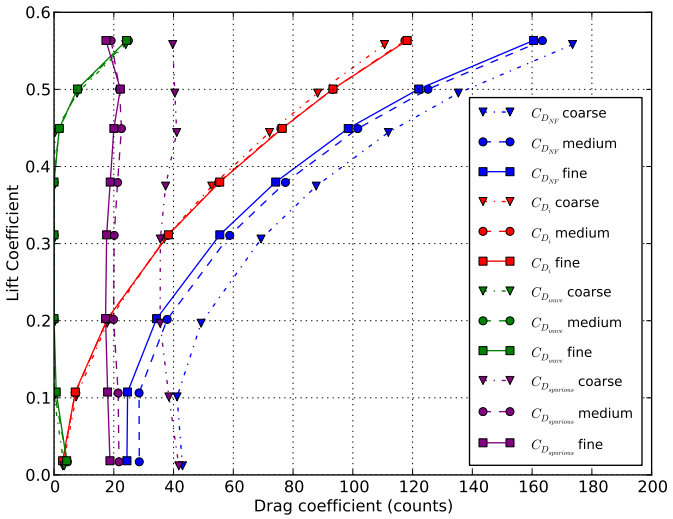

(a) Drag decomposition results

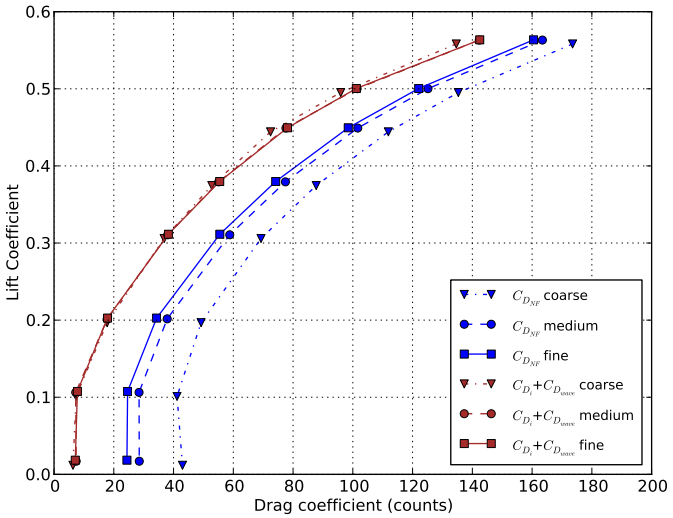

(b) Total drag results

Figure 4–5: Drag polars for DPW-W1 wing at $M = 0.76$

4.2 NACA 0012 Wing

This case represents the most complete of all discussed in this chapter. A thorough grid refinement study is performed at subsonic and transonic conditions. The three formulations of far-field induced drag are compared: Maskell's (Eq. (2.14)), Destarac's (Eq. (2.12)) and *Q-criterion* corrected induced drag (Eq. (2.15)). Sections 5.3 & 5.4 present aerodynamic shape optimizations for the same geometry and conditions studied in this section.

The baseline geometry is a rectangular wing that uses a NACA 0012-*modified* profile to have a sharp trailing edge. The description of the geometry can be found on the AIAA Aerodynamics Design Optimization Discussion Group (ADODG) case 3 [1]. The actual semispan length of the wing is $3.06c$ where c is the chord; the wing is rectangular over a semispan of $3.0c$ and enclosed by a wing-tip cap over the last $0.06c$. The wing-tip is comprised of a simple surface revolution based on the modified NACA 0012 profile. The reference semi-span area and semispan length are defined as $3c^2$ and $3c$ respectively.

A set of inviscid grid refinements comprising of 4 levels - supercoarse (baseline), coarse ($\times 2^3$ refinement), medium ($\times 3^3$), and fine ($\times 4^3$) - were used to discretize the flow domain. The grids were generated using the ICEM-CFD [23] meshing software. The grids are described in Table 4–1. A $C-O$ blocking topology is employed and the grids are refined up to 2 chords downstream to allow proper resolution of the trailing vortices.

Table 4–1: Grid Dimensions for NACA 0012-*modified* Wing (in root-chord units)

Level	Blocks	Grid Size (Nodes)	Spacing		Far-Field Distance
			Off-wall	Surface*	
Supercoarse	116	256,940	0.002	0.037	30
Coarse	116	1.82 M	0.001	0.019	30
Medium	116	5.89 M	0.00067	0.013	30
Fine	116	13.67 M	0.0005	0.009	30

* Estimated with $= \sqrt{S_{wet}/N_s}$, where S_{wet} and N_s are the wing wetted area and number of surface nodes respectively.

Figure 4–6 shows the structured grid elements on the wing surface and symmetry plane for the supercoarse grid. Particular attention was given to produce a smooth mesh at the wing-tip cap to ensure proper resolution of the wing-tip vortices.

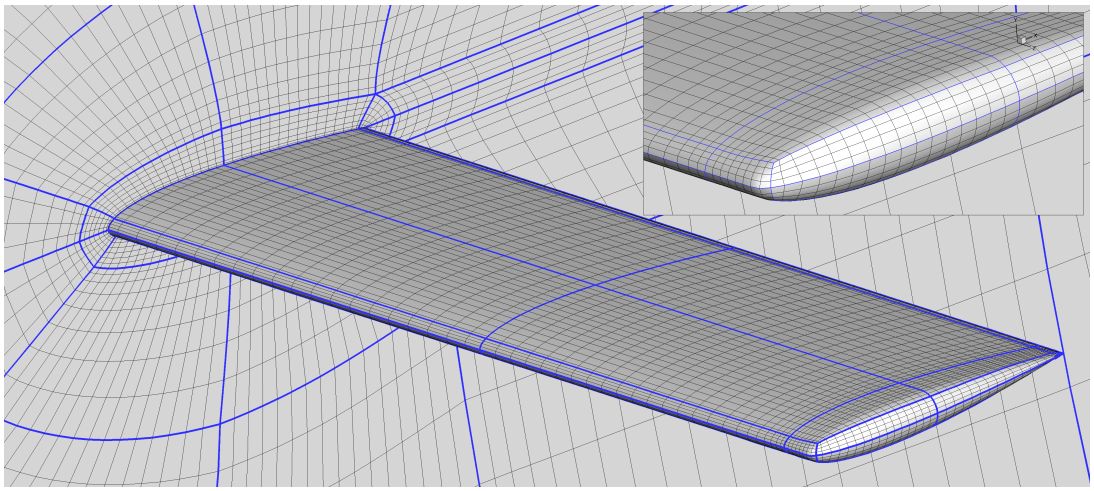

Figure 4–6: NACA 0012 Wing - Supercoarse Grid (enclosed top-right: zoom at wing-tip cap)

4.2.1 Inviscid Fully Subsonic - $M = 0.50$

Inviscid subsonic flow is first studied to investigate the various induced drag formulations; the only physical component of drag at such condition being induced

drag. The intent of this case is to observe and comment on any difference between the various formulations of far-field induced drag.

Figure 4–7 depicts the flow residual convergence for the 4 grid levels at $M = 0.50$ and $C_L = 0.375$. Convergence level approaches machine accuracy (10^{-16}) for all grids. Similar levels of convergence are reached for all flow conditions studied.

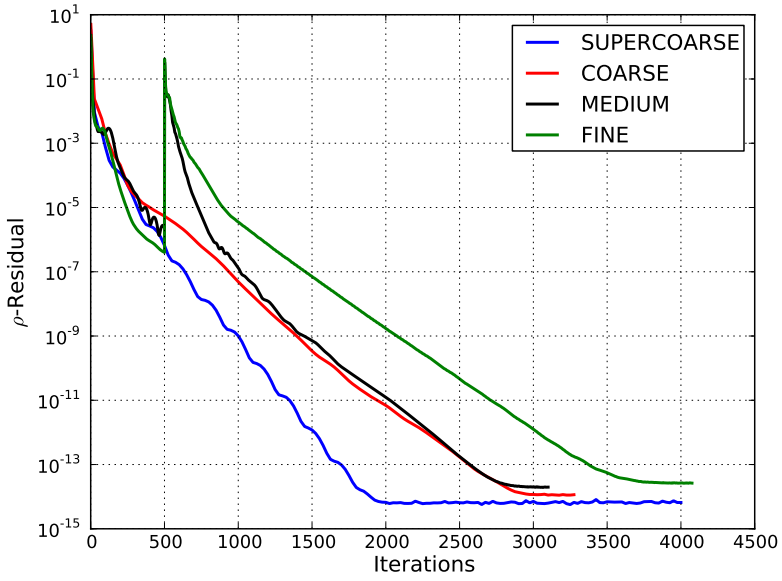

Figure 4–7: Untwisted NACA 0012-*modified* Wing: Residual convergence of flow solver on 4 grid levels at $M = 0.50$ and $C_L = 0.375$ ($||R_\rho||_1$ depicted)

Figure 4–8 shows the tip vortex and the lift distribution yielded by the coarse and fine grids at $M = 0.50$ and $C_L = 0.375$ corresponding to the flow condition of ADODG case 3 [1]. While little discrepancy is qualitatively observed in Figure 4–8, there is a significant variation in near-field drag between the two grid levels (∼4 drag counts). Figure 4–9 shows the volume generated by the *Q-Criterion* sensor; as expected, the vortex sensor appropriately captures the tip vortex (Figures 4–8(a)

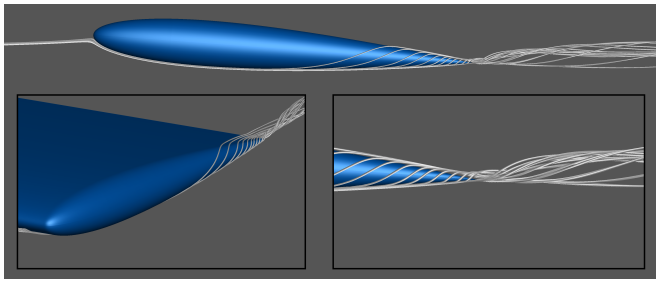

(a) Tip Vortex for Coarse Grid

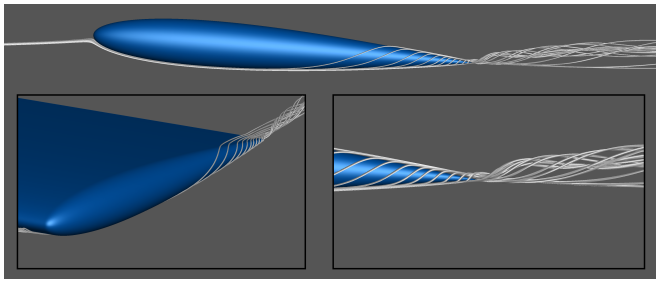

(b) Tip Vortex for Fine Grid

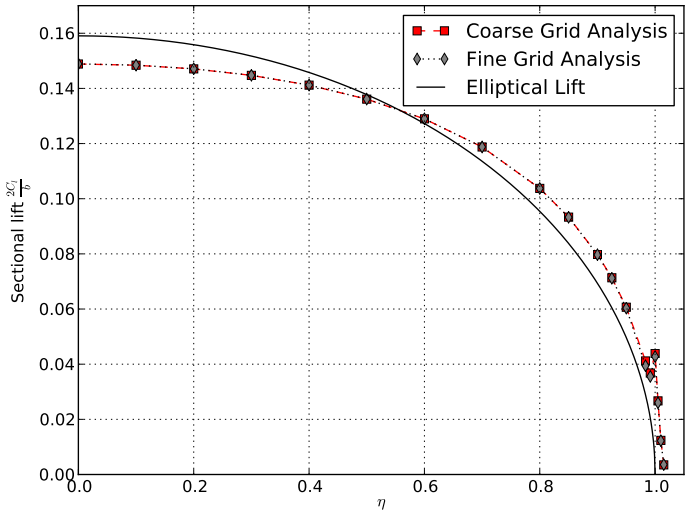

(c) Lift Distribution

Figure 4–8: Untwisted NACA 0012-*modified* Wing at $M = 0.50$ and $C_L = 0.375$ - Coarse and Fine Grids

& 4–8(b) for 3D streamlines at the wing tip). At this point, it may be important to re-emphasise that the *Q-Criterion* correction to the induced drag measures the *irreversible* drag generated inside the vortex volume and reassigns it to the induced drag. The assumption made is that the dissipation of the tip vortices, an *irreversible* process, is essentially due to numerical effects. For inviscid condition such as the one studied here, this assumption is particularly correct as viscous dissipation is absent.

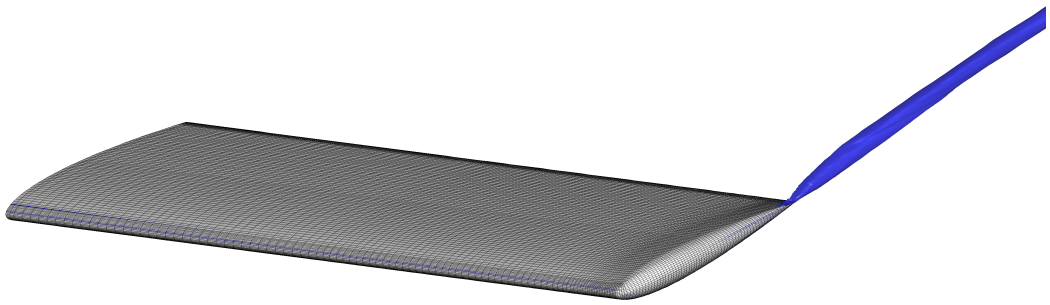

Figure 4–9: NACA 0012 Wing - Sample *Q-Criterion* volume on Medium Grid for $M = 0.50$ $C_L = 0.375$

The drag polars for the far-field drag components, and near-field drag are depicted in Figure 4–10(a). The implementation of Destarac's *irreversible* drag components (Eq. (2.6)) is employed. The various alternatives for induced drag - Destarac's C_{D_i}, crossflow plane integration $C_{D_{i-w}}$, and Destarac's with *Q-Criterion* correction $C_{D_{i-Q}}$- are shown in Figure 4–10(b). Figure 4–10(a) shows the spurious drag diminishing with grid refinements down to <1 drag count at the medium grid level. Spurious drag with the supercoarse grid exhibits non-trivial behaviour at low lift coefficient: the spurious drag measured is negative. The near-field drag yields similar negative drag values at low lift coefficient for the same grid. Considering that the wing is

symmetrical and, hence, drag should approach zero at zero lift, such behaviour is most likely attributable to numerical errors. All far-field induced drag formulations, on the other hand, consistently produce zero drag at zero lift condition.

Figure 4–11(a) compares drag polars for $C_{D_{i-Q}}$ and $C_{D_{NF}}$. The near-field drag shows a large variation with mesh sizing while the $C_{D_{i-Q}}$ varies by less than 2 drag counts. At the medium grid level, both polars for the medium grid are very similar (less than 1 count difference).

The mesh refinement for drag and span efficiency e at $C_L = 0.375$ are shown on Figure 4–11(b). The span efficiency is defined as,

$$e = \frac{C_L^2}{\pi \mathrm{AR} C_D}, \tag{4.1}$$

where AR is the wing aspect ratio. Considering that the rectangular wing hereby studied does not produce an elliptical lift distribution (see Figure 4–8(c)), its span efficiency is expected to be below 1.0, the theoretical optimum for planar wings.

All formulations of the induced drag show a reduced mesh dependency over traditional near-field drag ($\sim$2 counts variations for induced drag formulations versus $\sim$10 counts variation for the near-field drag). Moreover, the novel *Q-criterion* based correction allows for more consistent grid refinement convergence; by the medium grid both, $C_{D_{i-Q}}$ and $C_{D_{NF}}$, differ by less than 1 drag count. From the 3 induced drag formulations studied, the *Q-criterion* based induced drag is the only to produce a span efficiency value below 1.0 (at $\sim$0.98). It thus appears that the $C_{D_{i-w}}$, and C_{D_i} may still be underpredicting drag even at the fine grid level.

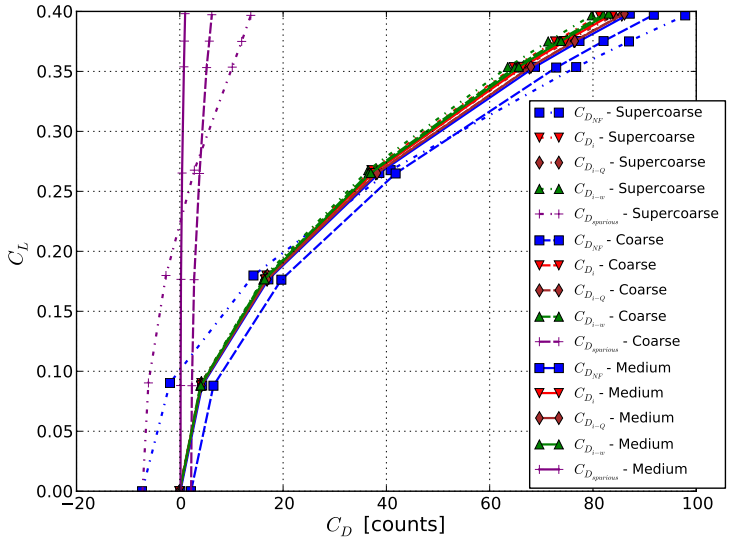

(a) Drag Polars for all Drag Components

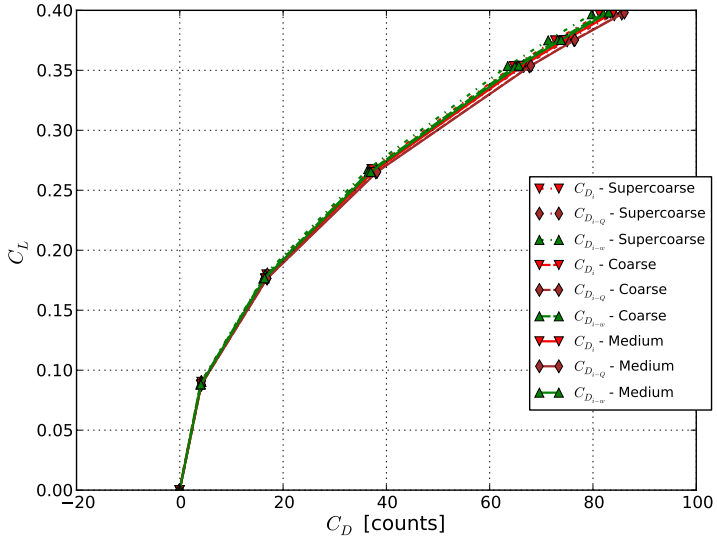

(b) Polars for Induced Drag Expressions

Figure 4–10: Drag Polars for NACA 0012-*modified* Wing at $M = 0.50$ (Part I)

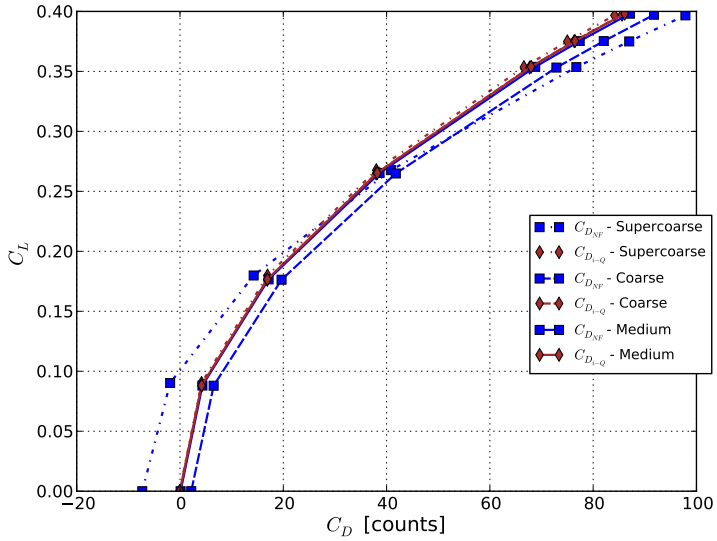

(a) Polars for $C_{D_{NF}}$ & $C_{D_{i-Q}}$

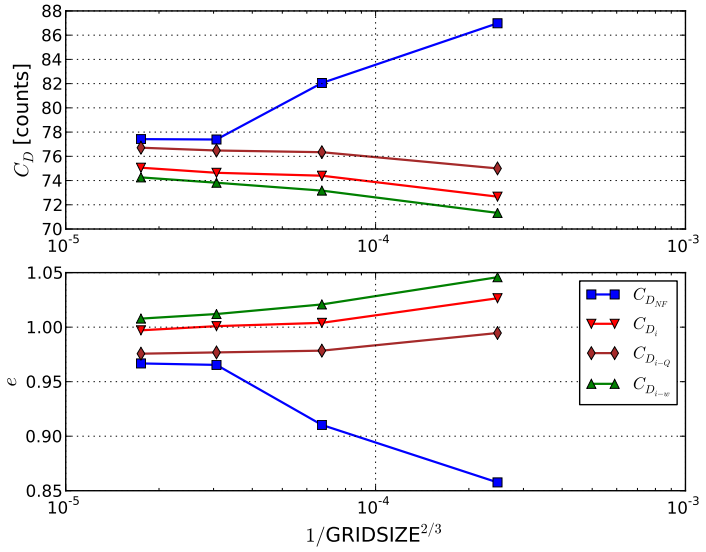

(b) Mesh Refinement Convergence at $M = 0.50$ & $C_L = 0.375$

Figure 4–11: Drag Polars for NACA 0012-*modified* Wing at $M = 0.50$ (Part II)

Results at $M = 0.50$ thus suggest that $C_{D_{i-Q}}$ is the most accurate and least mesh dependent of the three far-field induced drag formulations hereby studied.

4.2.2 Inviscid Transonic - $M = 0.70$

Using the same set of grids, a similar exercise was performed at a transonic speed, thus adding wave drag to the physical drag breakdown. One induced drag formulation, $C_{D_{i-Q}}$, is presented in this section for simplicity. Results are shown on Figures 4–12 and 4–13.

As presented in Section 4.1, the region defined by the shock detection function presented in Eq. (2.10) typically fails to capture all the generated entropy and any numerical oscillation at the vicinity of the shock. Again, a strategy similar to Ueno et al. [41] was used to extend the shock region originally defined by the shock detection function. This allows for a more consistent wave drag calculation, as shown by Figure 4–12(a), for a shock region extension of 5 or more. An extension to the shock region corresponding to 6 cells was selected for wave drag values presented in Figures 4–12(b), 4–13(a), and 4–13(b), and the optimization results presented in Section 5.4.

Figure 4–12(b) shows the near-field drag along with the far-field components of drag. The spurious drag again diminishes with grid refinements to below 1 drag count at the medium grid level. Wave drag (shown in pink) rises sharply for C_L greater than 0.3 as the larger angle-of-attack accelerates the flow on the upper surface of the wing and creates a shock wave (pressure contours for $C_L = 0.36$ are shown in Section 5.4). Wave drag differs by less than 1 drag count between the coarse and medium grids. As it was the case at $M = 0.50$, $C_{D_{i-Q}}$ shows very little mesh dependency ($\sim$

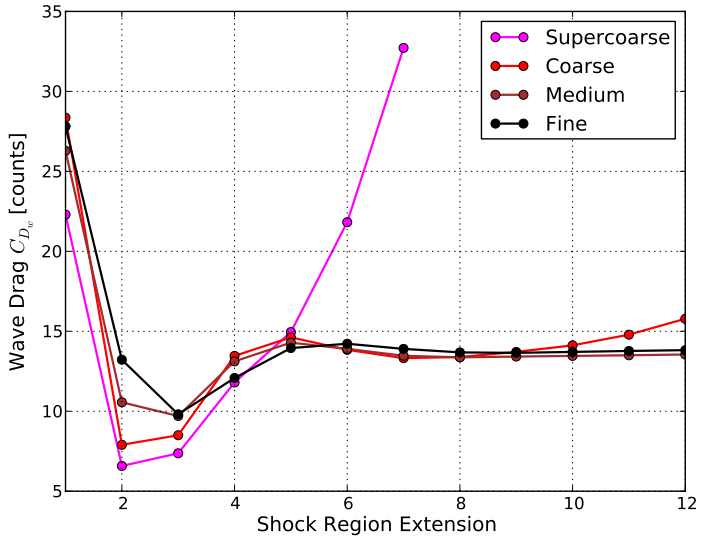

(a) C_{D_w} vs. Shock Region Extension at $\alpha = 3.5^o$

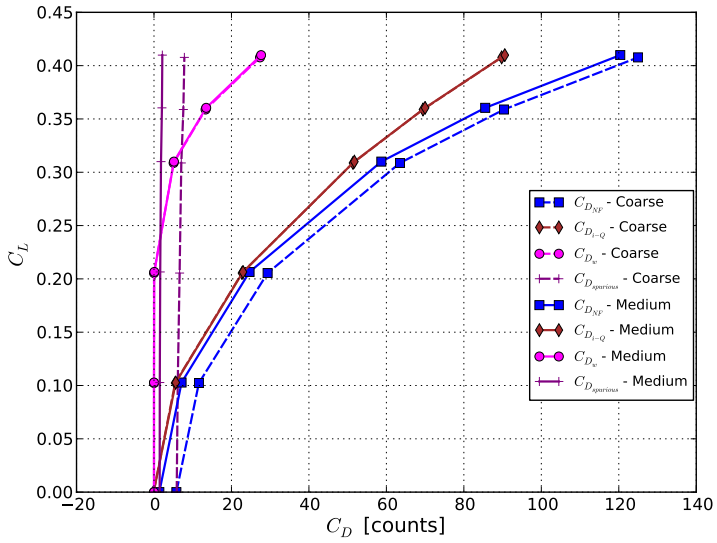

(b) Drag Polars for All Drag Components

Figure 4–12: Drag Polars for NACA 0012-*modified* Wing at $M = 0.70$ (Part I)

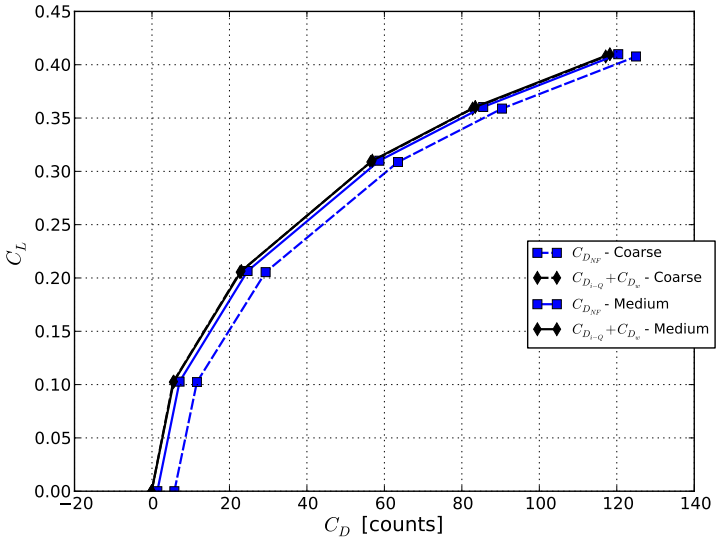

(a) Drag Polars for $C_{D_{NF}}$ & $C_{D_{i-Q}} + C_{D_w}$

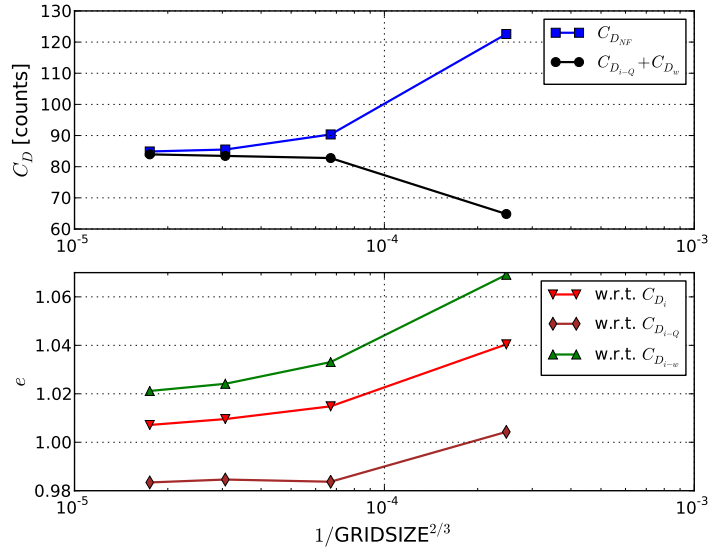

(b) Drag and Span Efficiency at $\alpha = 3.5^o$

Figure 4–13: Drag Polars for NACA 0012-*modified* Wing at $M = 0.70$ (Part II)

1 drag count). The near-field drag on the other hand varies by approximately 5 drag counts between the coarse and medium grids.

Figure 4–13(a) compares the drag polars of the sum of non-spurious far-field drag components (i.e. $C_{D_{i-Q}} + C_{D_w}$) and the near-field drag. Figure 4–13(b) shows the grid convergence for the total drag and the span efficiency at an angle-of-attack of 3.5^o; such angle-of-attack produces a lift coefficient approaching $C_L = 0.375$ studied in Section 4.2.1. As it was observed at $M = 0.50$, the far-field method is shown to be much less mesh dependent. The span efficiency calculated with respect to $C_{D_{i-Q}}$ is very similar to that obtained at $M = 0.50$ (i.e. 0.98) which is expected considering that span efficiency is theoretically independent of Mach and lift condition.

The implementation of the far-field drag decomposition is hereby shown effective in inviscid transonic conditions. Moreover, it is shown to be much less mesh dependent than the near-field approach.

4.3 CRM Isolated Wing - $M = 0.84$ $C_L = 0.500$

The CRM isolated wing geometry is described by ADODG case 4 [1]. This geometry corresponds to the isolated wing of the CRM wing-fuselage geometry defined by the Fourth AIAA Drag Prediction Workshop [3]. A pair of grids with a $C - O$ blocking topology was generated - with $837k$ and $6.19M$ nodes - to discretize the flow domain. The grids were generated using the ICEM-CFD [23] meshing tool. Fully viscous flow is studied.

Figure 4–14 shows a comparison of the pressure coefficient distribution for both grids. Little discrepancy is observed and the shock location is very similar for both grids, indicating that the resolution of the coarse grid may be sufficient for optimization purposes (design studies are carried on the coarse grid in Section 5.5). Figure 4–17 depicts flow residual convergence on the coarse grid; residual convergence down to $\sim 10^{-7}$ is observed.

Pressure coefficient contours and flow streamlines for the medium grid solution are depicted on Figure 4–15. A strong shock is observed on the upper surface of the wing; the shock spans from the wing root to about 2/3 of its span. Surface streamlines show no significant zone of separation, and the streamlines at the rounded wing-tip cap demonstrate proper resolution of the tip vortices.

A shock extension of 5 was used based on the shock extension sensitivity highlighted in Figure 4–16(a). Figure 4–18 shows sample viscous and shock regions for a shock extension of 5 on the coarse mesh. The drag values obtained are compared to published results from Lyu et al. [32] (MDO Lab at the University of Michigan), and Carrier et al. [12] (ONERA, France). The coarse and medium grids provided by

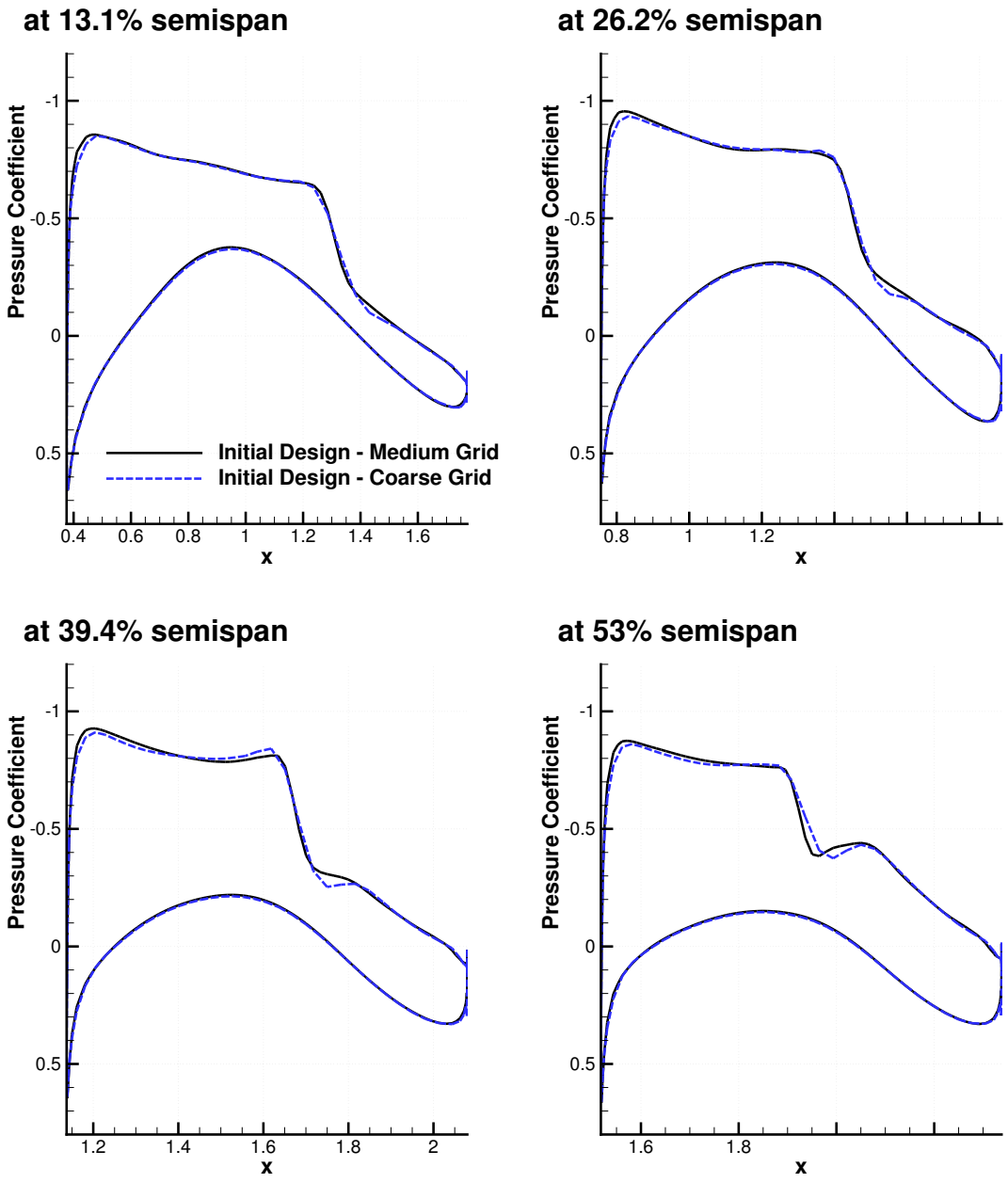

Figure 4–14: Coefficient of pressure on the CRM wing geometry for $M = 0.85$ and $C_L = 0.500$

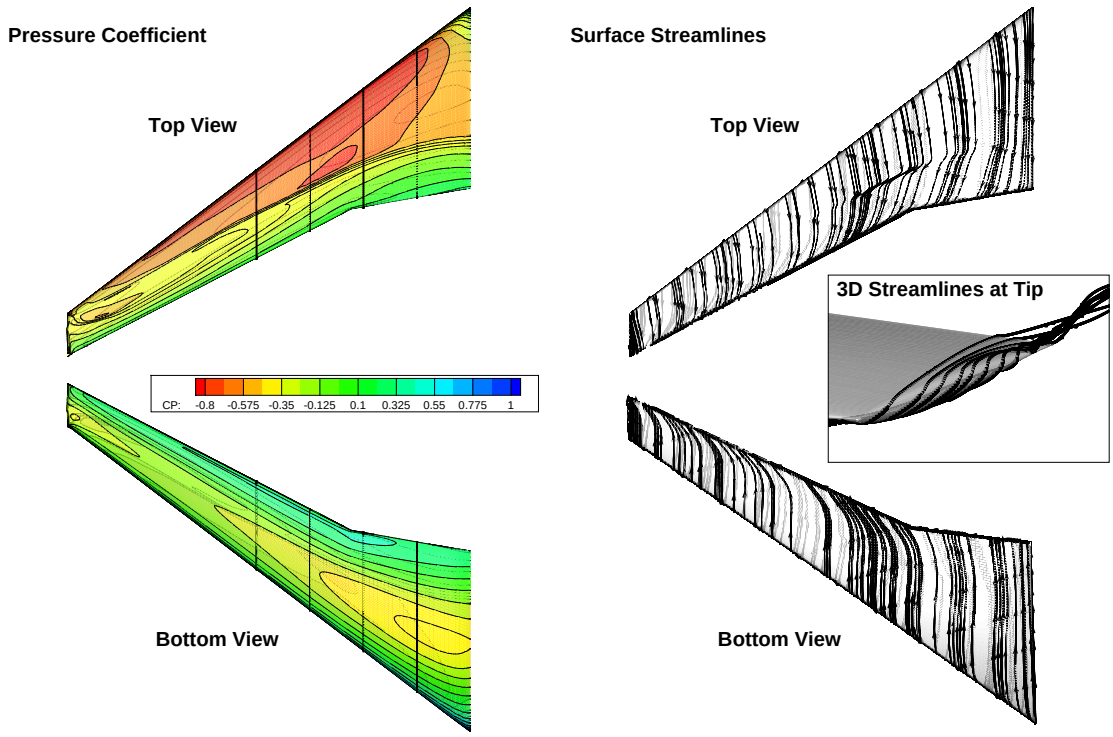

Figure 4–15: Contours of coefficient of pressure and Streamlines on the CRM wing geometry for $M = 0.85$ and $C_L = 0.500$ for Medium grid

the MDO Lab at University of Michigan were also solved using McGill University's *Computational Aerodynamics Group* solver (U.Michigan Grids/McGill Solver). Carrier et al. [12] provided decomposed components of drag using ONERA's *ff72* drag decomposition tool. Several drag components are compared in Table 4–2. More work will be done to validate the implementation of the far-field drag components in viscous flow. Supplemental cases will be studied including the full CRM wing-fuselage configuration where more detailed mesh refinement studies will be performed.

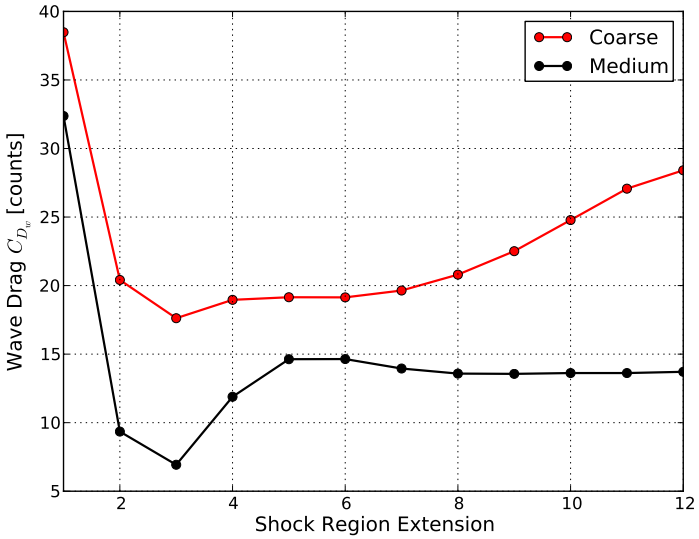

(a) C_{D_w} vs. Shock Region Extension

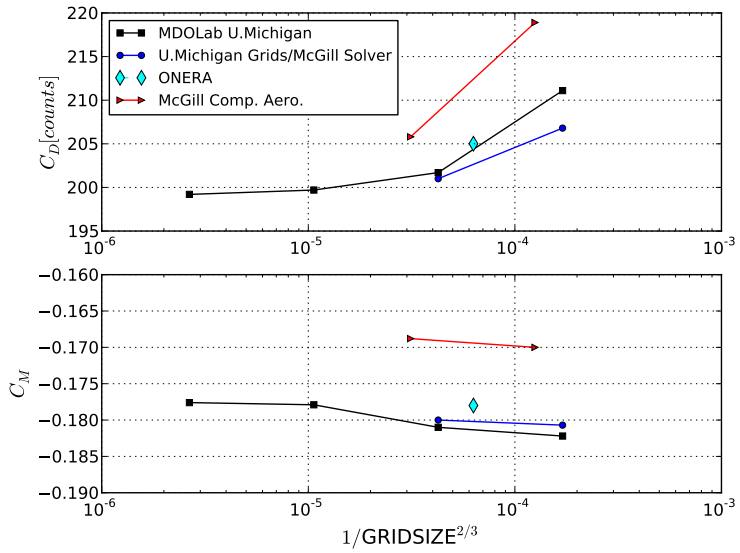

(b) Mesh Refinement Convergence

Figure 4–16: CRM wing geometry $M = 0.85$ and $C_L = 0.500$

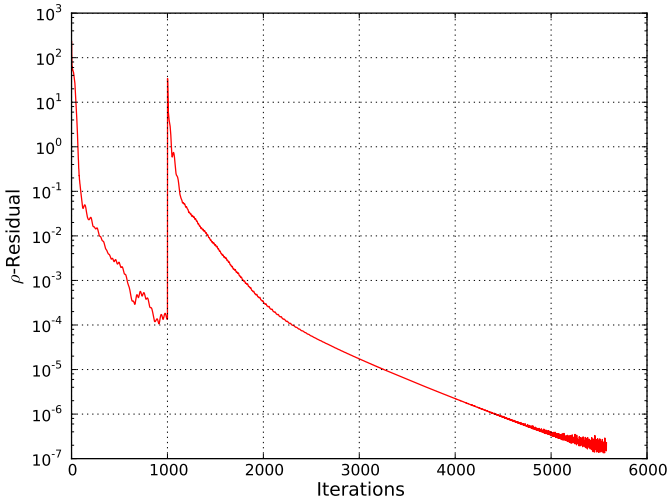

Figure 4–17: CRM wing geometry for $M = 0.85$ and $C_L = 0.500$: Residual convergence of flow solver for coarse grid ($||R_\rho||_1$ depicted)

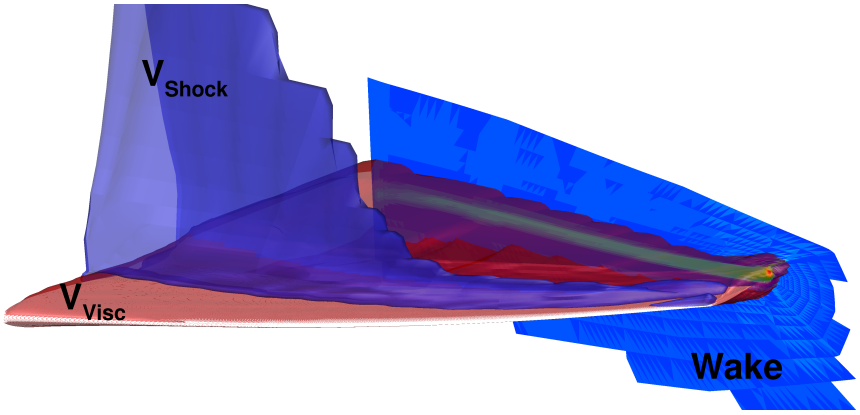

Figure 4–18: Sample $V_{viscous}$, V_{shock} (for shock extension of 5), and wake integration plane on the CRM wing geometry for $M = 0.85$ and $C_L = 0.500$ - Coarse grid

Table 4–2: CRM Wing Geometry Drag Components (in counts)

	$C_{D_{NF}}$	C_{D_p}	C_{D_f}	C_{D_i}	C_{D_w}
Coarse	218.9	157.0	62.0	96.4	18.9
Medium	207.8	149.2	58.5	97.6	14.6
ONERA [12]	205.0	145.3	59.7	95.9	8.5

CHAPTER 5
Optimization Results

Adjoint-based optimization using the far-field drag decomposition method is demonstrated on increasingly complex optimization cases in this chapter; several of the cases hereby presented refer to Bisson et al. [7, 8, 9, 10]. The main objective is to demonstrate the effectiveness of the employment of the drag decomposition approach for shape optimization. To this end, the effectiveness of the approach is also compared to optimizations driven by the standard *near-field* drag. Cases studied are increasingly complex. Their progression attempts to; first, minimize each drag component in isolated conditions and, second, perform optimization in conditions where different physical components are produced.

Particular attention is given to ADODG case 3 [1] as it represents a benchmark case of the aerodynamic shape optimization community. Furthermore, several induced drag formulations are presented in this thesis (including the novel *Q-criterion*) and this case allows the study of their relative performance in an adjoint-based optimization framework. Sensitivity of the optimization process with respect to the grid sizing is also discussed. Finally, ADODG case 4 (viscous) is presented for near-field drag driven optimization only, but future work will expand the investigation to the far-field drag components.

Table 5–1: NACA 0012 swept wing planform parameters

S_{ref}	Λ_{LE}	c_{root}	λ	$b/2$
$1.506m^2$	30^o	$0.8059m$	0.562	$1.1963m$

5.1 NACA 0012 Swept Wing Wave Drag Minimization

For a simple NACA0012 profile wing at zero-lift inviscid condition, unconstrained aerodynamic surface optimization was conducted. The optimization problem is posed as,

$$\text{minimize} \qquad C_D \text{ w.r.t. } x \in \mathbb{R}^n,$$

where the near-field drag ($C_{D_{NF}}$), or the wave drag (C_{D_w}) from Kusunose's formulation (Eq. (2.8)) are used as the objective functions. The focus of this case is to explore the ability of the proposed approach for a simple shock mitigation problem: a more complex shock mitigation problem follows in Section 5.4. Given the simplicity of the optimization problem posed, a simple steepest descent optimization strategy is employed in this section.

5.1.1 Geometry and Parametrization

A uniformly tapered and sweptback wing using the NACA 0012 airfoil cross-section was used as the initial geometry. The planform reference parameters are defined in Table 5–1.

The wing surface is parametrized using a set of 14 B-spline control points in the streamwise direction and 12 B-spline control points in the spanwise direction (i.e., 14×12 control points). The set of control points is depicted on Figure 5–1. The parametrization and associated sensitivities are obtained using CAD engine pyPSG

[27]. The computations are performed over a structured C-grid of $198 \times 48 \times 48$. For Mach 0.83 (where a moderate strength shock is observed on the wing) and zero-lift condition (i.e., at $\alpha = 0.0^o$), a shock across the wing span is produced (see Figure 5–4). In the absence of lift, the only components of drag for the case studied are wave and spurious drags.

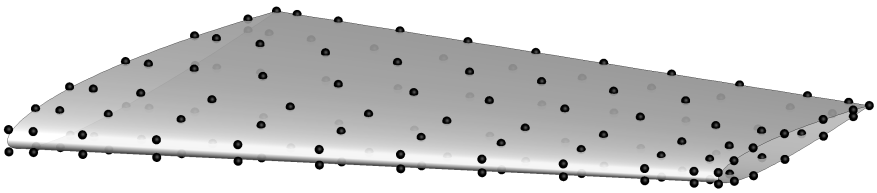

Figure 5–1: NACA0012 Swept Wing: Control points (black) of B-Spline parametrization

5.1.2 Results

Residual convergence of the flow and adjoint solvers is depicted on Figure 5–2; where both figures demonstrate convergence levels approaching machine accuracy (10^{-16}).

Since the only physical component of drag acting is wave drag, the two approaches are expected to produce similar results. Table 5–2 shows the initial and final drag coefficients. The optimization driven by the wave drag fully removes the wave drag C_{D_w} and produces a total drag $C_{D_{NF}}$ within 1 drag count of that produced by the optimization driven by the near-field drag. The evolution of near-field and wave drags through the design iterations are depicted on Figure 5–3. It should be noted that, for this particular case, the number of design iterations corresponds to the

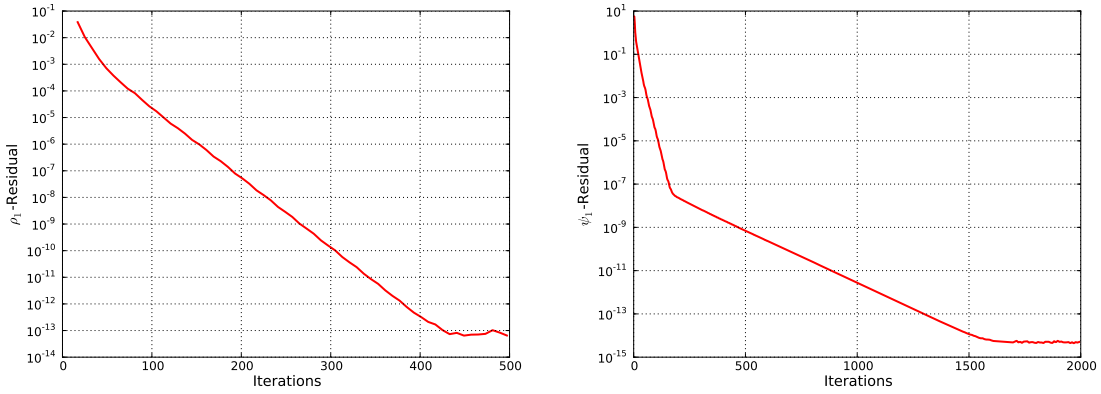

(a) $||R_\rho||_1$ (b) $||R_{\psi_1}||_1$

Figure 5–2: NACA 0012 Swept Wing: Residual convergence of flow and adjoint solvers

number of function evaluations, since a fixed step length was employed. The green curves denote optimization driven by the near-field drag while the blue curves represent optimization driven by the wave drag. The wave drag approach appears to outperform slightly the near-field by approximately 1 drag count on both measures of drag ($C_{D_{NF}}$ and C_{D_w}). Both optimizations were assumed terminated within 17 design iterations.

The initial and final pressure contours are shown on Figure 5–4. Both methods successfully removed the pressure discontinuity. Interestingly, each approach produced a slightly different pressure contour while both produce similar final drag values. The reason why the two approaches did not yield the exact same design is yet to be determined and will be as part of a future work.

By definition, the adjoint solution represents the sensitivities of the objective function with respect to perturbations in the residual. Figure 5–5 shows the contour

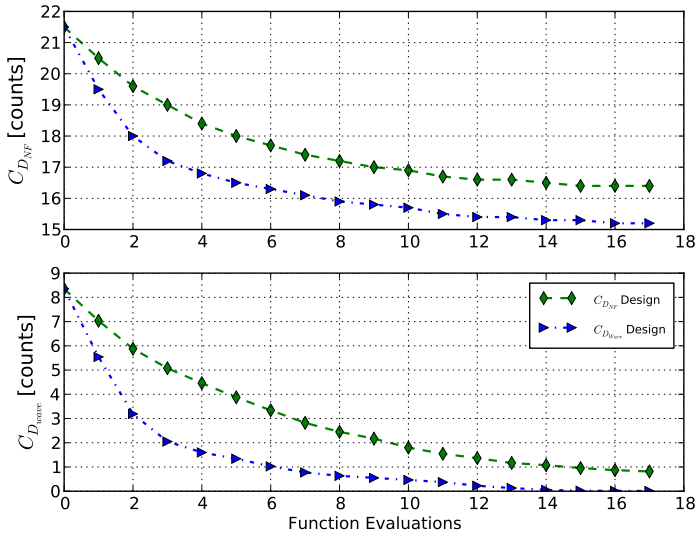

Figure 5–3: NACA 0012 Swept Wing: Drag components versus function evaluations for adjoint-based optimization with near-field drag and wave drag objective functions

Table 5–2: NACA0012 Swept Wing optimization results for $M = 0.83$ and $C_L = 0.00$

	$C_{D_{NF}}$	$C_{D_{\Delta s}}$	C_{D_w}
Initial Geometry	0.0022	0.0022	0.0008
Near-Field Design	0.0016	0.0016	0.0001
Wave Drag Design	0.0015	0.0015	0.0000

at 84.8% semi-span of the fifth adjoint solution (ψ_5 which related to the conservation of energy) at the first iteration when the wave drag is the objective function. The variation of the adjoint solution is localized at the shock region boundaries demonstrating that the optimization will search for design changes that affects the flow in this region. The adjoint solution does not present any significant variation inside and well outside of the shock region.

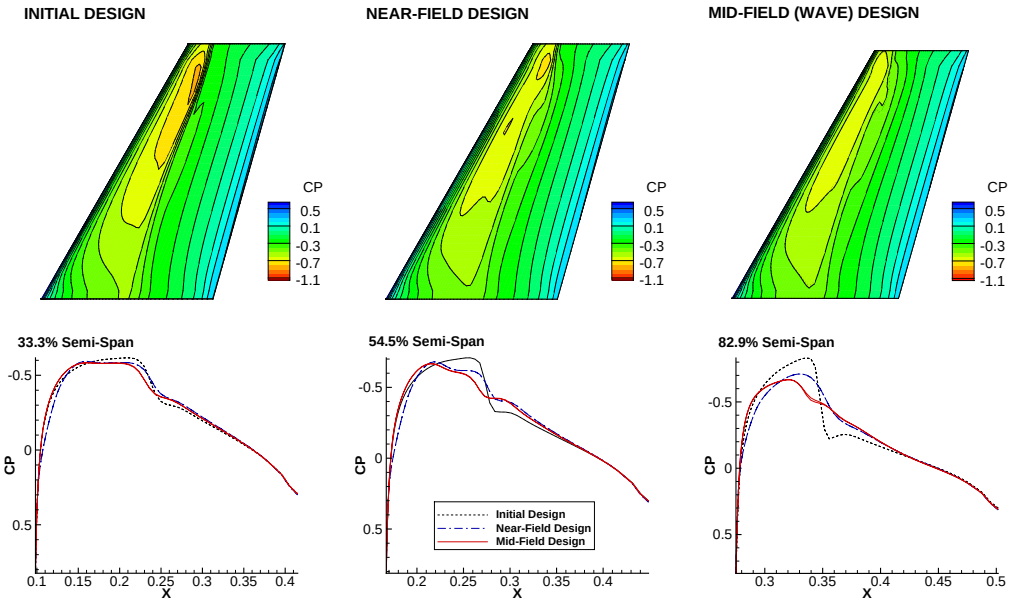

Figure 5–4: NACA 0012 Swept Wing: Comparison of pressure contours at $M = 0.83$ and $C_L = 0.0$ for adjoint-based optimization with near-field drag and wave drag objective functions

For the wave drag optimization results presented in this thesis, the adjoint and gradient source terms were obtained by linearising the surface integration over the shock volume defined in Eq. (2.6). However, the linearisation did not explicitly consider the shock detection function that defines the shock volume. It was preliminary assumed that such simplification would have a insignificant effect on the gradient accuracy. For future work, an effort to include the linearisation of the shock detection function in the adjoint and gradient derivations will be considered which could

potentially lead to more accurate gradients. A possible alternative is to define an expression for wave drag that includes the shock detection function. If implemented, the assumption made as part of this work may be verified.

Nevertheless, this section demonstrates the effectiveness of the proposed approach for shock mitigation in inviscid flow; while sections 5.4 and 5.5 demonstrate more complex cases where this case is repeated in inviscid and viscous flows with the addition of constraints. Industrial relevant cases will be considered as part of future work.

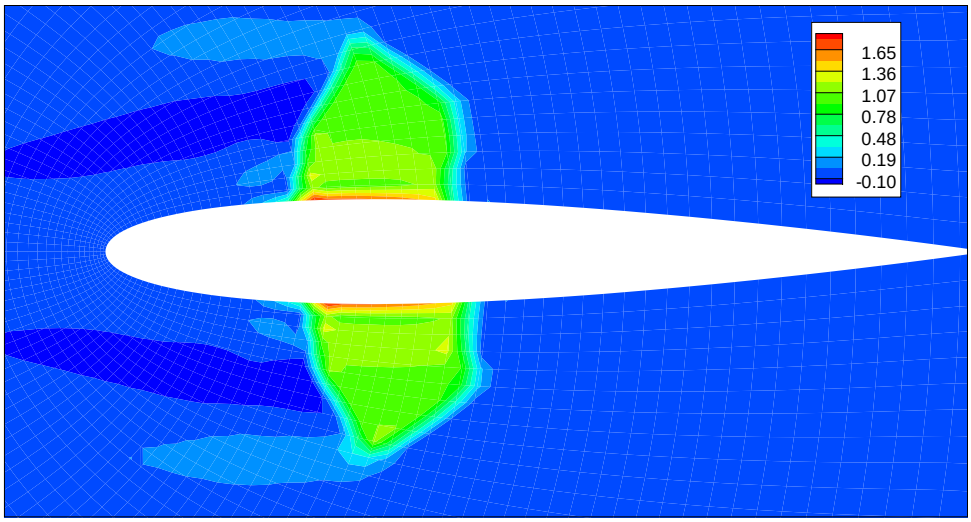

Figure 5–5: NACA 0012 Swept Wing: ψ_5 adjoint contour at 84.8% semi-span for wave drag as objective function

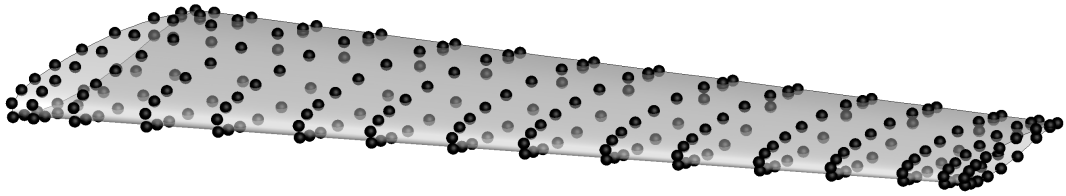

Figure 5–6: DPW-W1 wing B-spline parametrization

5.2 DPW-W1 Wing Induced Drag Minimization

This section shows the induced drag minimization in both subsonic and transonic conditions. The constrained optimization problem examined in this section is posed as,

$$\begin{aligned} \text{minimize} \quad & C_D \text{ w.r.t. } x \in \mathbb{R}^n \\ \text{subject to} \quad & |C_L - C_{L_{Target}}| \leq 0.005, \end{aligned}$$

where x denotes the design variables. Optimization driven by near-field coefficients ($C_{D_{NF}}$, $C_{L_{NF}}$) and far-field coefficients ($C_{D_{i-w}}$, $C_{L_{wake}}$) are compared. This case is the only in this chapter that presents a drag minimization optimization problem driven by Maskell's induced drag formulation (Eq. 2.14).

5.2.1 Geometry and Parametrization

The DPW-W1 wing was used as the initial geometry, and parametrized with 18×16 B-spline control points. Drag decomposition for the initial geometry was assessed in Section 4.1. Each spanwise set of control points is free to rotate about the fixed trailing edge, i.e. the design variables are the effective angles-of-attack at each of the 16 spanwise set of control points.

The medium grid presented in Section 4.1 is used as it provides the best compromise between accuracy and computational cost. Figure 5–7 depicts a sample convergence plot of the adjoint solver residual for a transonic condition presented in Section 5.2.3: final residual approaches machine accuracy (10^{-16}).

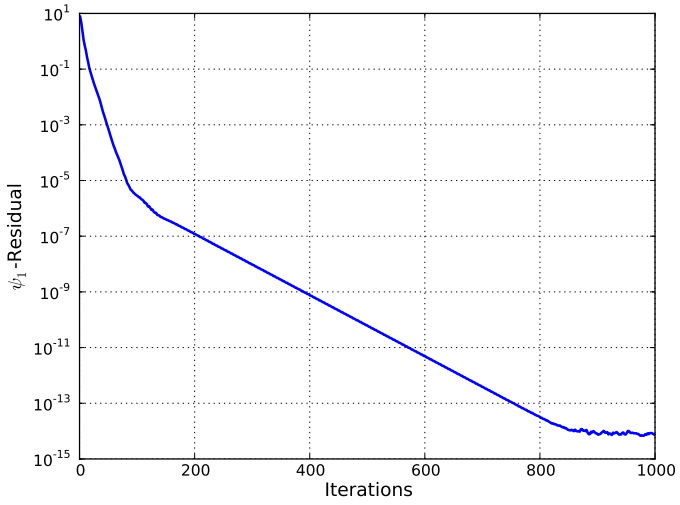

Figure 5–7: DPW-W1 at $M = 0.76$ and $C_L = 0.500$: Sample residual convergence of adjoint solver for medium grid ($||R_{\psi_1}||_1$ depicted)

5.2.2 Optimization Results for Subsonic Condition

In this subsection, a Mach number of 0.60 at $C_{L_{target}} = 0.400$ was used yielding subsonic flow throughout the domain. Therefore, the only physical component of drag is induced drag effectively meaning that the near-field drag and the induced drag driven optimizations are expected to yield similar designs.

Figure 5–8 shows the evolution of lift and near-field drag coefficients for both approaches. The lift coefficient is maintained well within the prescribed bounds for the induced drag approach, while the bound is active for the near-field approach.

$C_{D_{NF}}$ is reduced by 1 to 2 drag counts. The relative improvement of the span efficiency e, defined in Eq. (5.1), with respect to the span efficiency of the initial geometry e_o was used to evaluate the effectiveness of the different approaches.

$$e = \frac{C_L^2}{\pi AR\, C_D}, \tag{5.1}$$

where, $AR = b^2/S_{ref}$ is the aspect ratio, and b the span. The near-field drag $C_{D_{NF}}$ and induced drag $C_{D_{i-w}}$ are separately employed to evaluate the span efficiency. The relative improvement of span efficiency e through the design iterations is shown by the upper and lower plots of Figure 5–10(b). The green curves denote the optimization driven by near-field drag, while the blue curves depict the optimization driven by induced drag. A 2.5% increase in span efficiency is achieved for both optimization approaches.

The trends for the upper and lower curves of Figure 5–10(b) are similar. This is an expected behaviour since the only physical component of drag in subsonic flow is induced drag. Relying on $C_{D_{i-w}}$ to compute the relative improvement in span efficiency is most notably useful in transonic conditions. In these conditions, the usage of $C_{D_{NF}}$ is inappropriate for span efficiency considerations due to the fact that an amount of wave drag is produced by shock waves.

The span loadings presented on Figure 5–10(a) show that the geometries produced by both approaches (near-field drag and induced drag minimizations) compare well against the theoretical elliptical lift distribution from lifting-line theory.

Figure 5–11 shows iso-surfaces of the third and fourth adjoint solutions (corresponding to the vertical and spanwise momentum equations respectively) at the first

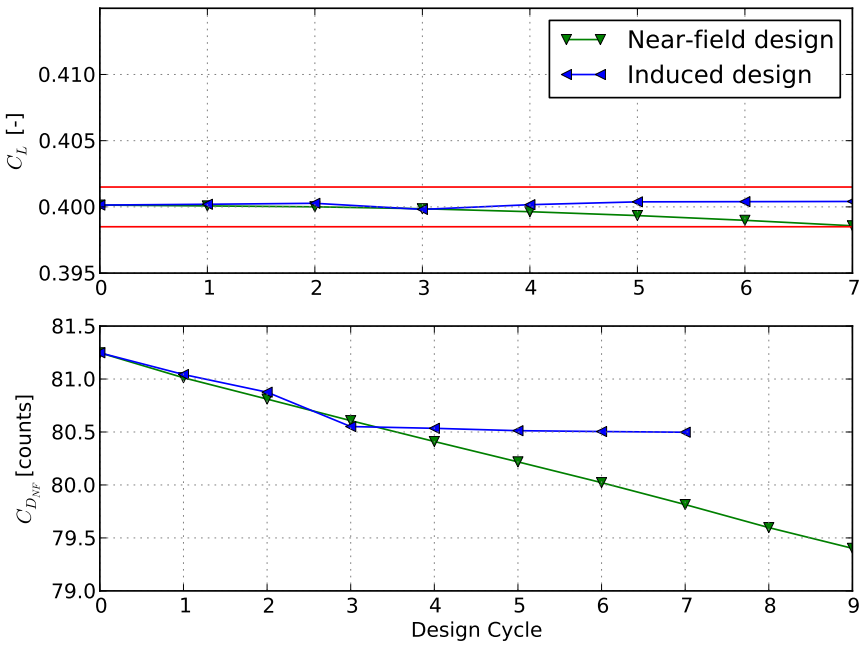

Figure 5–8: DPW-W1 at $M = 0.60$ at $C_{L_{target}} = 0.400$ - C_L and $C_{D_{NF}}$ with respect to design cycle (major iterations steps)

iteration with the induced drag as the objective function. Both figures show that a perturbation to the tip geometry, results in variations to the surrounding flowfield, and has the largest effect on Maskell's induced drag. This behaviour is expected as the vortices produced at the wing tip are typically stronger.

In conclusion, in subsonic condition, the induced drag driven optimization has shown similar effectiveness to that demonstrated by the near-field drag. The resulting designs for both approaches are very similar in terms of span efficiency and lift distribution.

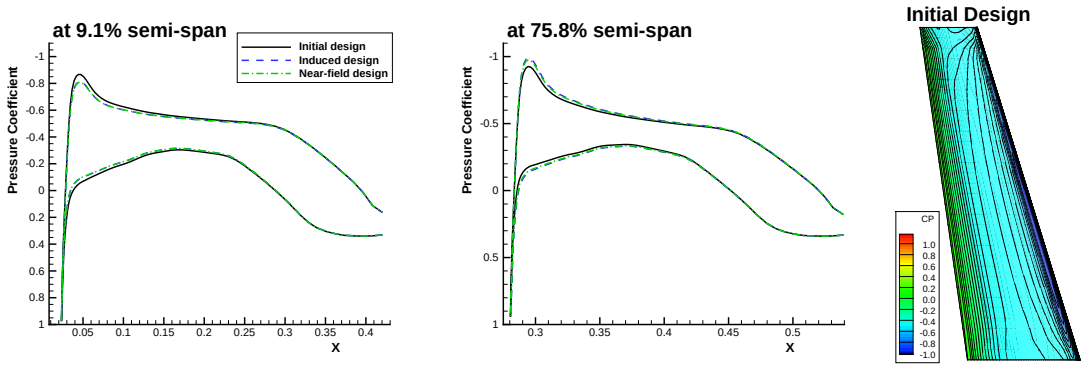

Figure 5–9: DPW-W1 $M = 0.60$ at $C_{L_{target}} = 0.400$ - wing pressure coefficient for initial and final designs

5.2.3 Optimization Results for Transonic Conditions

For the same geometry, constrained optimization of induced drag has been applied to several transonic conditions, presented in Figures 5–12(a) & 5–12(b), to show the isolated effects of the induced drag driven optimization in transonic condition. The objective of this section is to highlight the ability of the proposed approach to threat each phenomenological component of drag independently, i.e. for this specific case, to minimize the induced drag without regard to the strength and location of the shock waves produced. While it may not have industrial need for the design of an aircraft wing, the ability of the drag decomposition approach to determine how the various aspects of the wing contribute towards the total drag coefficient may be insightful for designers.

Figure 5–13 shows the evolution of lift and the variation of the drag components ($\Delta C_{D_{NF}}$, and $\Delta C_{D_{i-w}}$ expressed with respect to initial geometry) through the major iteration steps. Lift is maintained within the bounds, and the objective function ($C_{D_{i-w}}$) is reduced for all conditions; up to 5 counts reduction is observed at $M = 0.80$

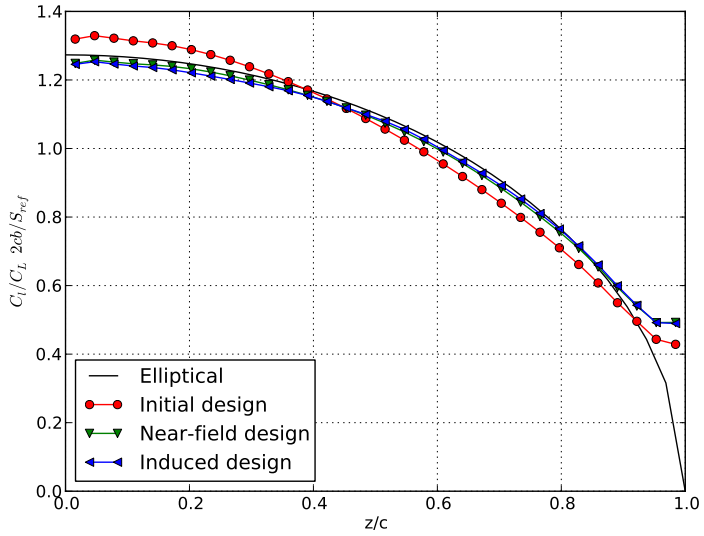

(a) Span loading

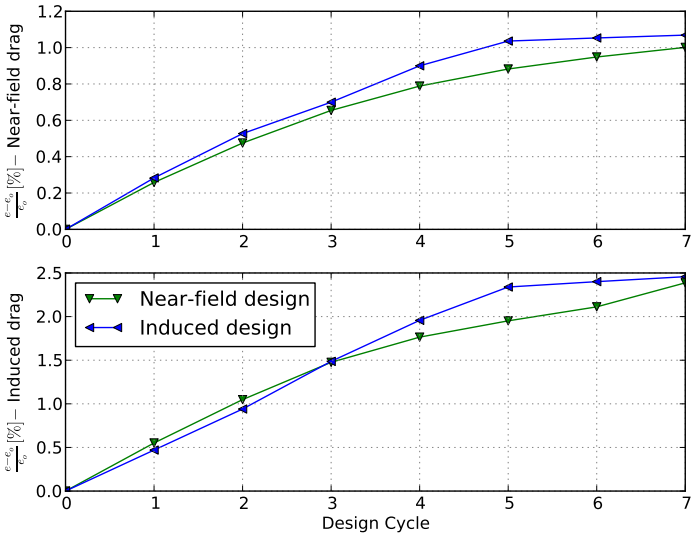

(b) Efficiency

Figure 5–10: DPW-W1 wing constrained drag minimization at $M = 0.60$, and $C_L = 0.400$

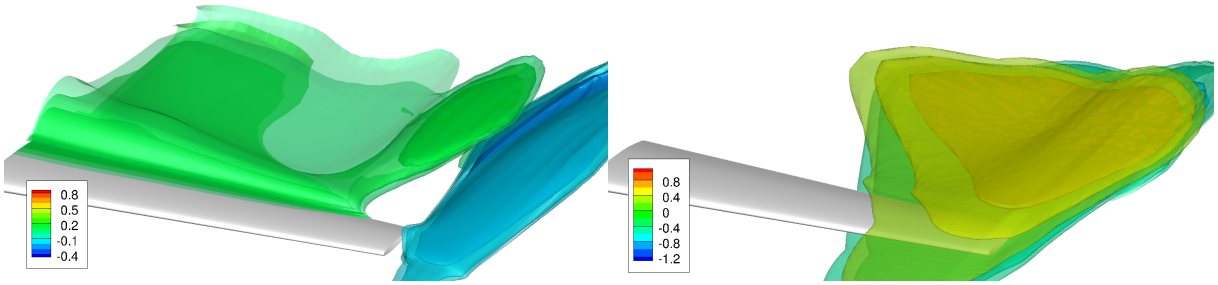

(a) ψ_3 (b) ψ_4

Figure 5–11: DPW-W1 wing ψ_3 and ψ_4 iso-surfaces for $M = 0.60$, and $C_L = 0.400$ with induced drag as objective function

& $C_L = 0.400$. It should be noted that the variation to the total near-field drag ($\Delta C_{D_{NF}}$ which comprises the sum of induced, wave and spurious drags) does not necessarily equal the induced drag reduction. In fact at $M = 0.76$ & $C_L = 0.500$, the induced drag decreases by more than 3 drag counts while the near-field drag slightly increases. This can be explained by the wave drag rising on the final design as a collateral effect of the induced drag driven optimization. This further shows the ability of the proposed method to threat each phenomenological component of drag independently.

Figure 5–14(a) shows the span loading from the final geometries obtained for all conditions studied in this section. The relative improvement of the span efficiency e through the design iterations is shown on Figure 5–14(b) for each condition. The final span loadings approached the theoretical elliptical lift distribution, and the span efficiency e is improved by nearly 2.5% to 3.0% for all studied conditions.

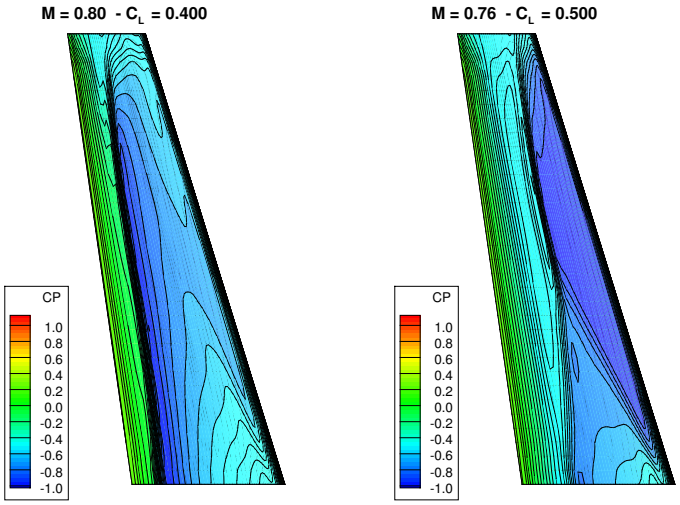

(a) Pressure distribution for transonic conditions

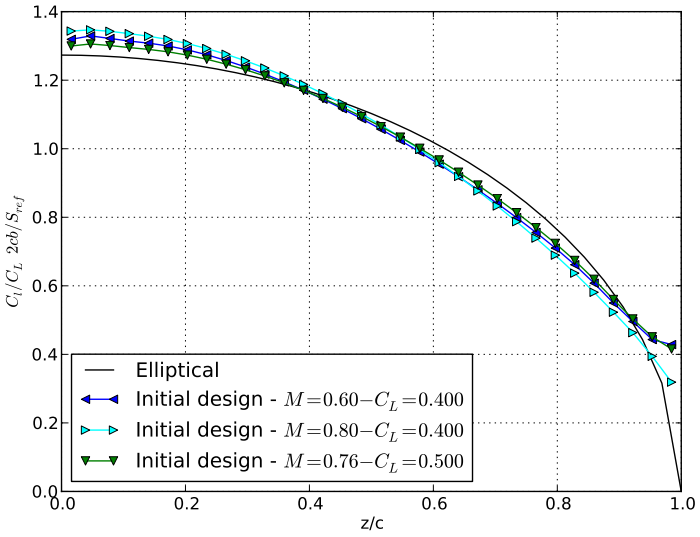

(b) Span loading

Figure 5–12: DPW-W1 wing initial conditions at subsonic and transonic conditions

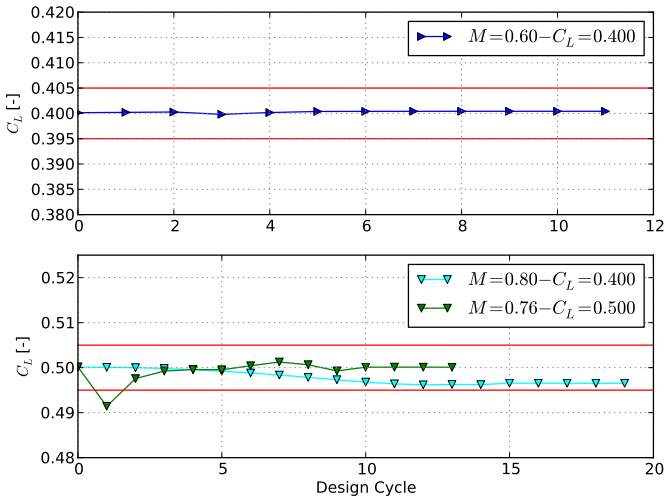

(a) Lift coefficient

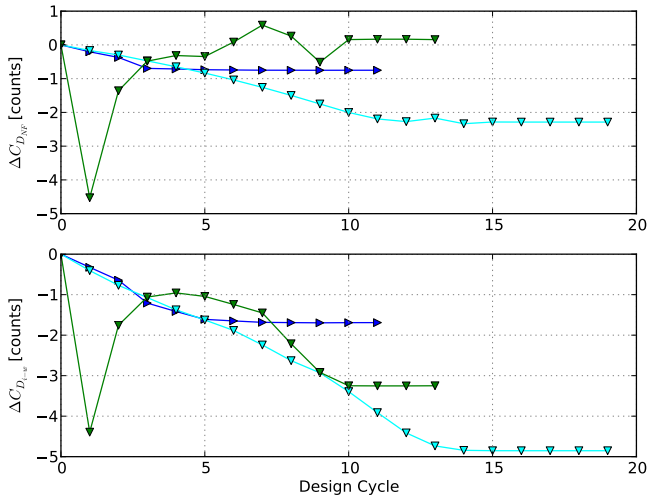

(b) $\Delta C_{D_{NF}}$ and $\Delta C_{D_{i-w}}$

Figure 5–13: DPW-W1 wing - Optimization evolution subsonic and transonic conditions with induced drag as objective function

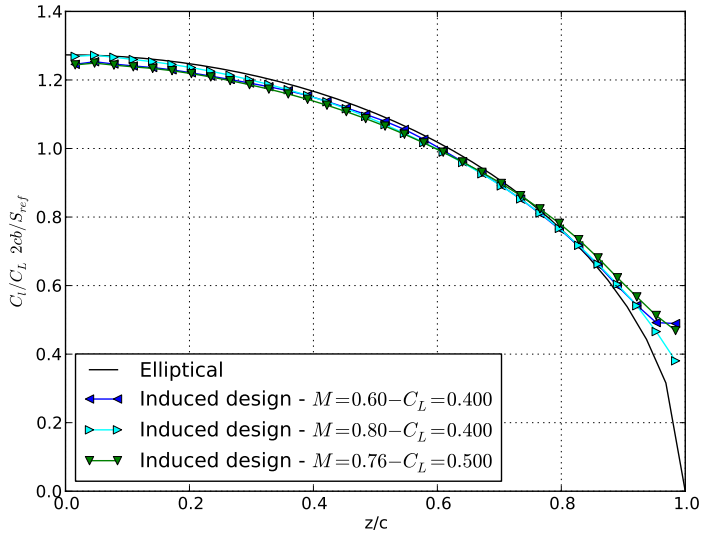

(a) Span loading

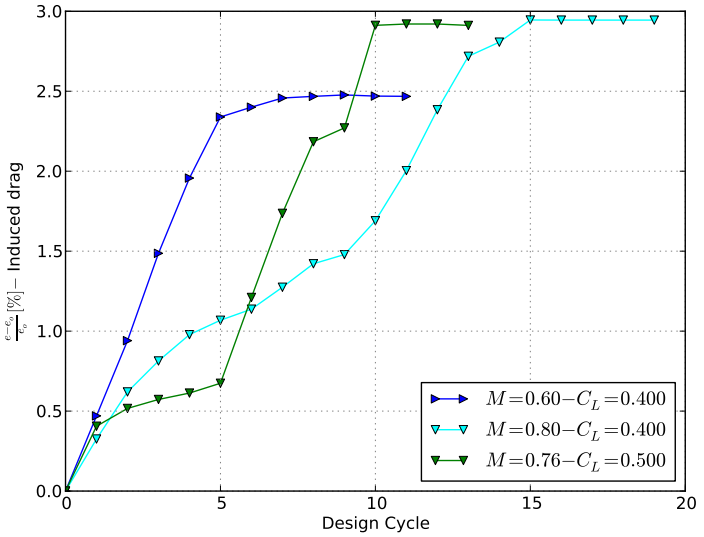

(b) Efficiency

Figure 5–14: DPW-W1 wing constrained induced drag minimization at subsonic and transonic conditions

5.3 Twist Optimization of the NACA 0012 Wing in Subsonic Inviscid Flow

To further assess the effectiveness of the proposed approach for induced drag minimization, the following optimization problem, based on the ADODG case 3 [1], was posed as,

$$\begin{aligned} \text{minimize} \quad & C_{D_{NF}} \text{ or } C_{D_i} \text{ or } C_{D_{i-Q}} \\ \text{w.r.t.} \quad & \gamma \\ \text{subject to:} \quad & |C_L - 0.3750| \leq 0.0001, \end{aligned}$$

where $C_{D_{NF}}$, C_{D_i}, $C_{D_{i-Q}}$, and C_L are the near-field drag, Destarac's induced drag, Destarac's induced drag with *Q-criterion* based correction, and the lift coefficients respectively. The design variable is the twist distribution, γ, about the trailing edge of the wing. The Mach number is fixed at 0.50, and the fluxes were evaluated through the JST scheme. The optimization is considered converged when the SNOPT optimality condition reaches 10^{-6} while the design satisfies the lift constraint. A mesh refinement study was performed in detail for the same geometry in the previous chapter (Section 4.2).

5.3.1 Parametrization

The parametrization method used for this particular case relies on a support spline defined as,

$$P(t) = \begin{bmatrix} x(t) \\ y(t) \\ z(t) \\ \gamma_z(t) \\ Scal(t) \end{bmatrix}, \tag{5.2}$$

where $P(t)$ represents the vector of position (x, y, z), angular rotation about the spanwise axis (γ_z), and scaling factor $(Scal)$. This parameterization method was found particularly interesting to perform large planform deformation of wings using a limited set of design variables. Figure 5–15 shows an arbitrary deformation of the Onera M6 wing using such a parameterization; where all 5 dimensions of 4 equally spaced control points along a support spline located at the trailing edge were arbitrary varied.

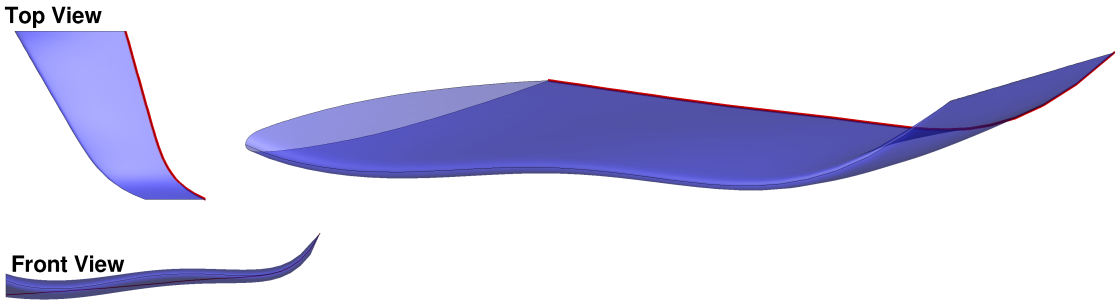

Figure 5–15: Sample deformation on the Onera M6 wing for an arbitrary modification to support spline control points in all 5 dimensions

For the particular optimization case presented in this section, only the $\gamma_z(t)$ dimension is modified through the optimizations and the support spline is placed at the trailing edge of the NACA 0012 rectangular wing; effectively, the design space is the twist distribution along the trailing edge. The spline is parameterized using Bernstein basis functions [38].

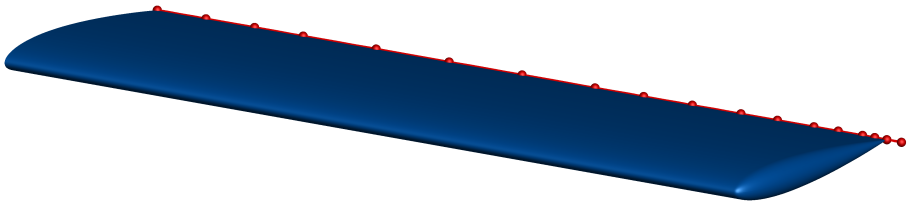

Figure 5–16: Baseline NACA 0012-*modified* Wing Geometry and Parametrization Spline (Red)

A total of 18 control points are distributed along the trailing edge of the baseline geometry. The control points are clustered near the tip where the largest twist is expected. Figure 5–16 shows the baseline wing along with the support spline and the control points distribution.

The rate of change of twist at the tip was implicitly constrained by attaching the last two control points, located at $z = \{3.0, 3.06\}$, to a single design variable as employed by Hicken et al. [20]. This limits the modifications to the wing-tip cap thus preventing exploitation of nonphysical separation effects.

5.3.2 Results - Coarse Grid

A sample adjoint residual convergence is depicted on Figure 5–17. The achieved convergence level is not as good than for the previous cases: the residual stalls at

10^{-5} approximately. The reason for the premature stalling of the adjoint residual is believed to be attributable to the resolution of the flow at the wing-tip trailing edge. This region was particularly challenging for the numerical solver; the maximum residual was localized to that region.

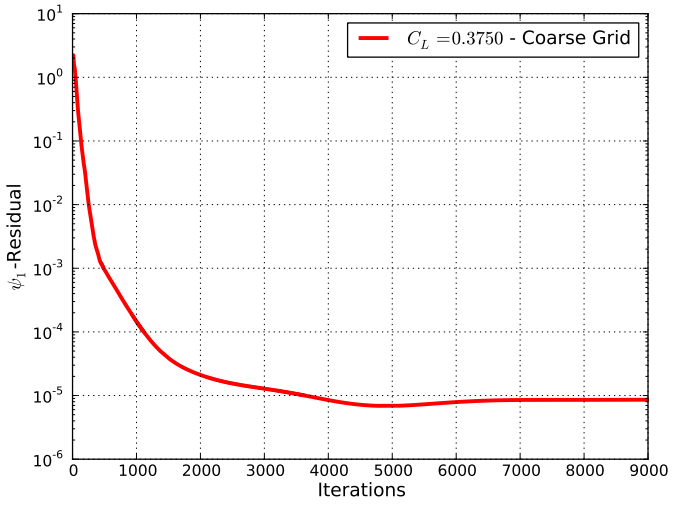

Figure 5–17: NACA 0012-*modified* Wing at $M = 0.50$ and $C_L = 0.375$: Sample residual convergence of adjoint solver for the coarse grid ($||R_{\psi_1}||_1$ depicted)

The constrained optimizations for $C_{D_{NF}}$, C_{D_i}, and $C_{D_{i-Q}}$ were first performed on the coarse grid described in Table 4–1. Figure 5–18 shows the SNOPT optimality condition and the lift coefficient as a function of the major iterations. It should be noted that for all results presented in this section the number of major iterations matches the number of function evaluations.

For C_{D_i} and $C_{D_{i-Q}}$ driven designs, the optimality condition drops below 10^{-6} thus satisfying the prescribed convergence criteria. For $C_{D_{NF}}$, SNOPT fails to bring the optimality below the predetermined threshold; however, any further function calls

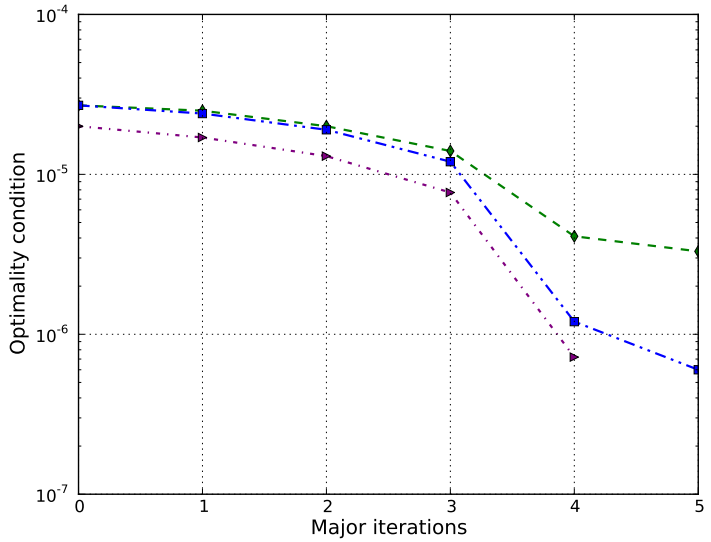

(a) Optimality

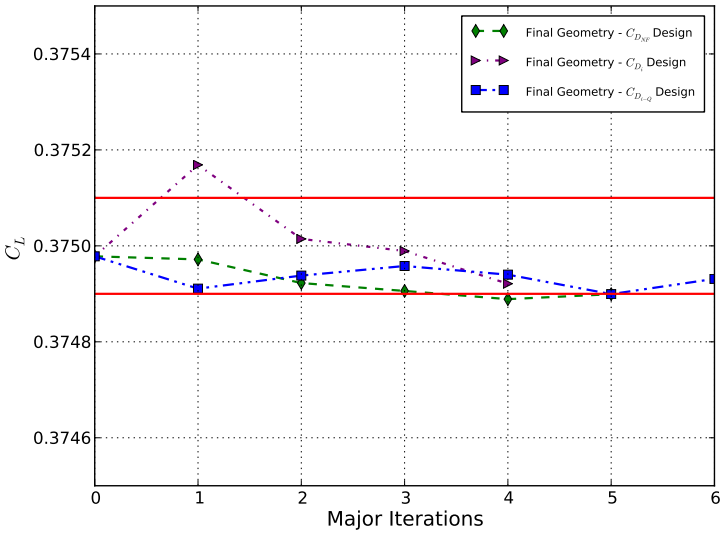

(b) Lift w.r.t. to function calls

Figure 5–18: Twist Optimization evolution for NACA 0012-*modified* Wing at $M = 0.50$ and $C_L = 0.375$ - Coarse Grid

Table 5–3: Drag, Lift and Span Efficiency of the Untwisted and Optimized NACA 0012-*modified* Wings - Coarse Grid Optimization

	Initial	Optimized w.r.t $C_{D_{NF}}$	Optimized w.r.t C_{D_i}	Optimized w.r.t $C_{D_{i-Q}}$
C_L	0.37498	0.37490	0.37492	0.37493
$C_{D_{NF}}$ [counts]	85.5	84.4	84.4	84.4
C_{D_i} [counts]	74.2	73.7	73.6	73.7
$C_{D_{i-Q}}$ [counts]	76.2	75.0	75.0	75.0
e w.r.t. $C_{D_{NF}}$ [%]	87.28	88.35	88.32	88.35
e w.r.t. C_{D_i} [%]	100.60	101.13	101.27	101.14
e w.r.t. $C_{D_{i-Q}}$ [%]	97.93	99.42	99.39	99.42

saw a very slight variation to the twist distribution (in the order of 0.0001^o ensuing variation to the objective function in the order of 0.05 drag counts), the optimization for $C_{D_{NF}}$ was assumed practically terminated.

Figures 5–19 shows the drag coefficients, and span efficiencies with respect to the major iterations. The green, purple, and blue curves depict $C_{D_{NF}}$ driven design, C_{D_i} driven design, and $C_{D_{i-Q}}$ driven design respectively. All three approaches yield very similar convergence rates, and final drag values. It should be noted that all three designs produce a span efficiency approaching the theoretical optimum of 1.0 (at ~ 0.995) when span efficiency is expressed with $C_{D_{i-Q}}$.

The final lift and twist distributions for the different approaches are depicted on Figure 5–20. The designs for $C_{D_{NF}}$ and $C_{D_{i-Q}}$ produce very similar twist distributions while the design for C_{D_i} yields a lower twist at the tip.

The final span efficiency, lift and drag coefficient values are tabulated in Table 5–3. Table 5–4 shows the initial and final sectional lift and twist at specific spanwise stations.

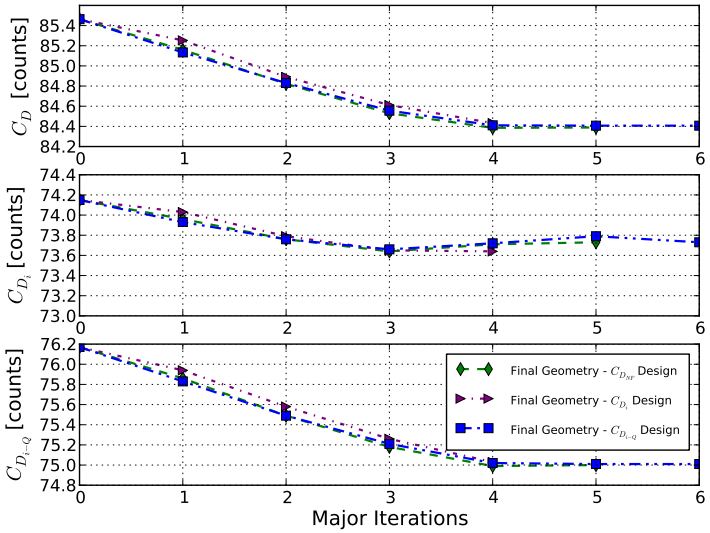

(a) Drag Components

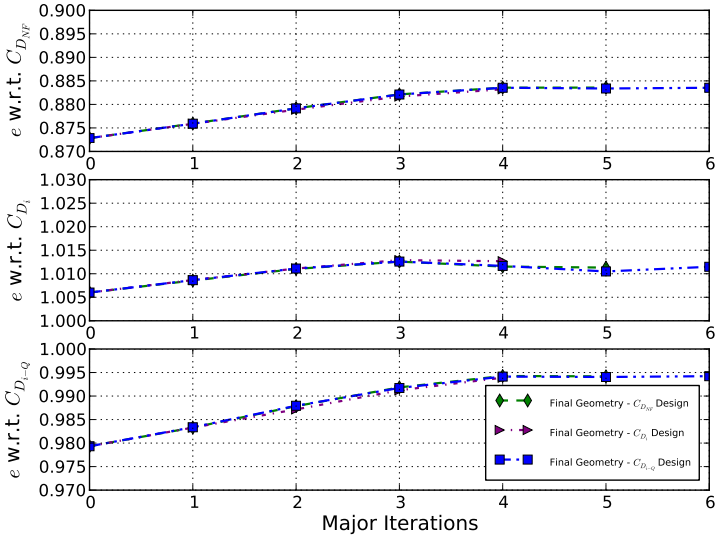

(b) Span Efficiency

Figure 5–19: Twist Optimization for NACA 0012-*modified* Wing at $M = 0.50$ and $C_L = 0.375$ - Coarse Grid (Part I)

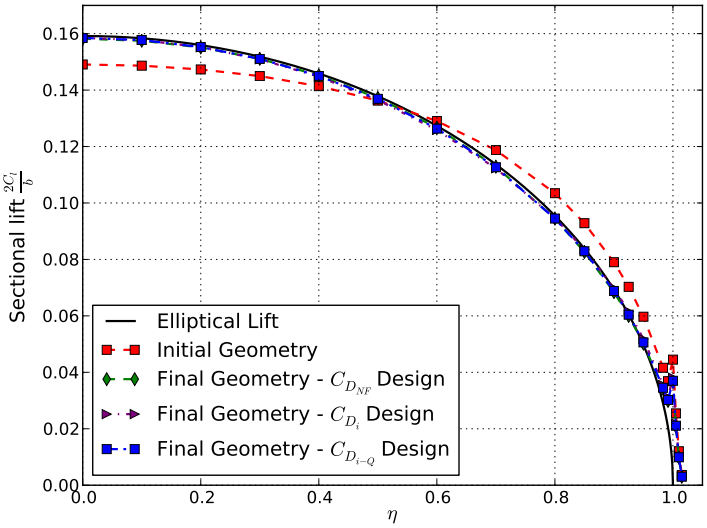

(a) Lift Distribution

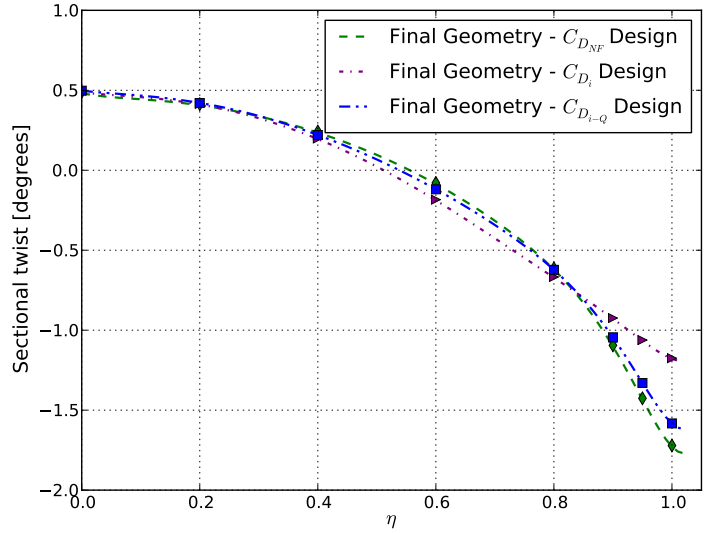

(b) Twist Distribution

Figure 5–20: Twist Optimization for NACA 0012-*modified* Wing at $M = 0.50$ and $C_L = 0.375$ - Coarse Grid (Part II)

Table 5–4: Twist and Sectional Lift of the Optimized NACA 0012-*modified* Wings - Coarse Grid Designs

	η	0.0	0.2	0.4	0.6	0.8	0.9	1.0
γ [^{o}]	$C_{D_{NF}}$ Opt.	0.4897	0.4135	0.2420	-0.0790	-0.6134	-1.0947	-1.7212
	C_{D_i} Opt.	0.4912	0.4153	0.1990	-0.1840	-0.6672	-0.9242	-1.1750
	$C_{D_{i-Q}}$ Opt.	0.4975	0.4210	0.2204	-0.1191	-0.6226	-1.0446	-1.5830
$2C_l/b$	$C_{D_{NF}}$ Opt.	0.1582	0.1551	0.1452	0.1267	0.0944	0.0502	0.0366
	C_{D_i} Opt.	0.1585	0.1552	0.1447	0.1258	0.0946	0.0518	0.0381
	$C_{D_{i-Q}}$ Opt.	0.1585	0.1552	0.1450	0.1263	0.0945	0.0506	0.0370

At the coarse grid level, all three approaches are practically shown equivalent; final designs and convergence rates are similar. The proposed approach was thus shown effective at performing wing planform optimization for both C_{D_i}, and $C_{D_{i-Q}}$.

5.3.3 Results - Supercoarse Grid

This subsection studies the same optimization problem and applies the same three approaches as presented in the previous subsection but, this time, using the supercoarse grid to discretize the domain. The objective is to assess the mesh dependency of each approach, and determine if any procures a relative advantage over the others.

The SNOPT optimality condition along with the lift coefficient throughout the major iterations are depicted (Figure 5–21). The lift is again shown within predetermined bounds for all three approaches. Optimizations for $C_{D_{NF}}$ and $C_{D_{i-Q}}$ are shown to converge to the convergence threshold. The optimization driven by C_{D_i} shows a great reduction in optimality condition but fails to fully satisfy the convergence threshold. As for the case of $C_{D_{NF}}$ on the coarse grid, the optimization was determined converged as any ensuing modifications to the twist distribution are very minor and have a negligible impact on the objective function and lift constraint.

Figure 5–22 shows the evolution of each drag components, and span efficiencies through the major design iterations. As it was the case with the coarse grid results, all three approaches exhibit similar convergence rate and final drag and span efficiency values.

However, a significant difference is observed on the twist distribution. Figure 5–23(b) shows a difference of approximately 1.0^o at the tip between the three approaches. It should be noted that the final twist distribution for C_{D_i} differs by up to $\sim 1.0^o$ from the final design obtained with the coarse grid. Designs for $C_{D_{NF}}$ and $C_{D_{i-Q}}$ are more consistent with the designs obtained on the coarse grid; they differ by less than 0.4^o and 0.2^o respectively. This further suggests that an optimization for

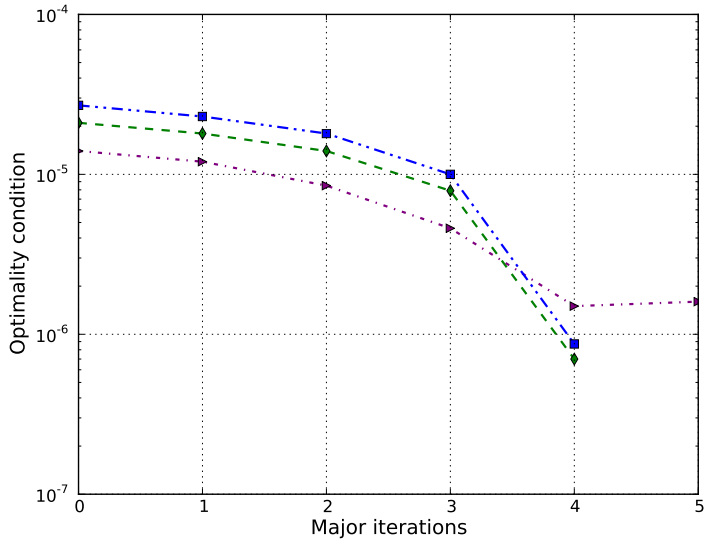

(a) Optimality

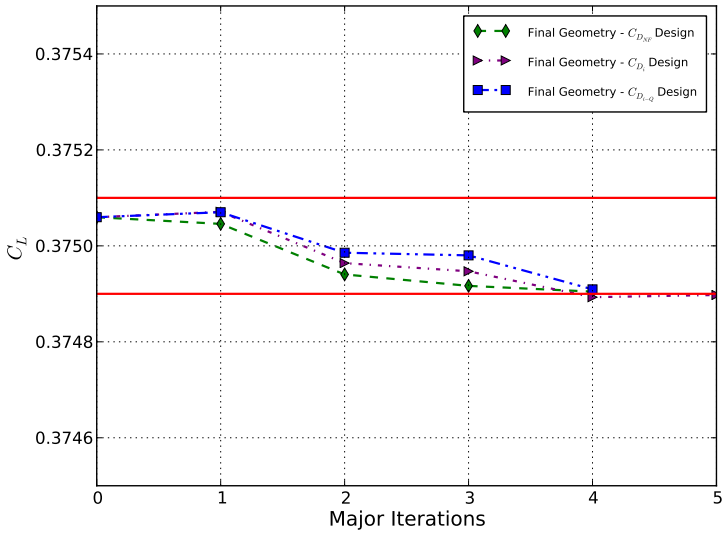

(b) Lift w.r.t. to function calls

Figure 5–21: Twist Optimization for NACA 0012-*modified* Wing at $M = 0.50$ and $C_L = 0.375$ - Supercoarse Grid

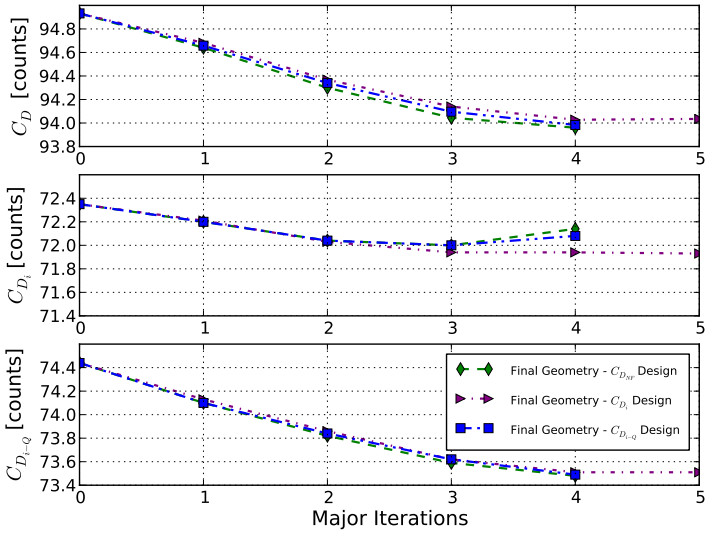

(a) Drag Components

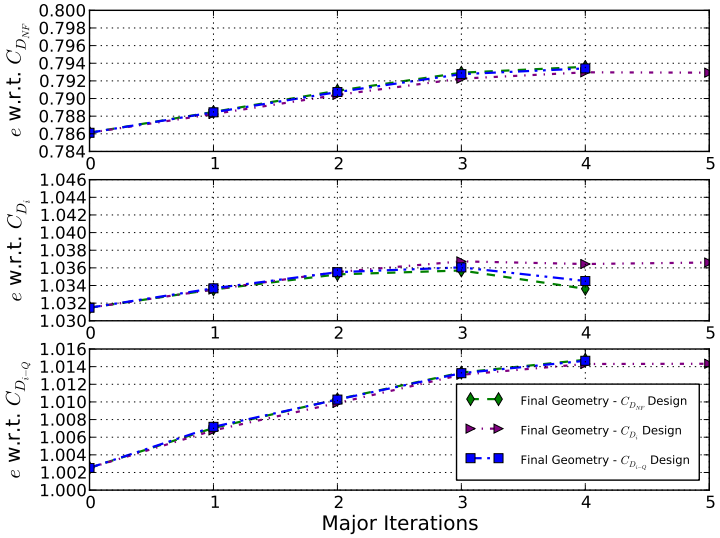

(b) Span Efficiency

Figure 5–22: Twist Optimization for NACA 0012-*modified* Wing at $M = 0.50$ and $C_L = 0.375$ - Supercoarse Grid (Part I)

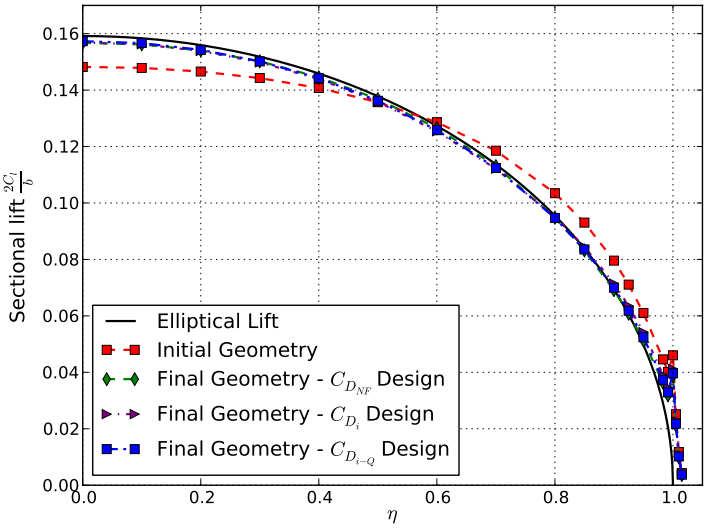

(a) Lift Distribution

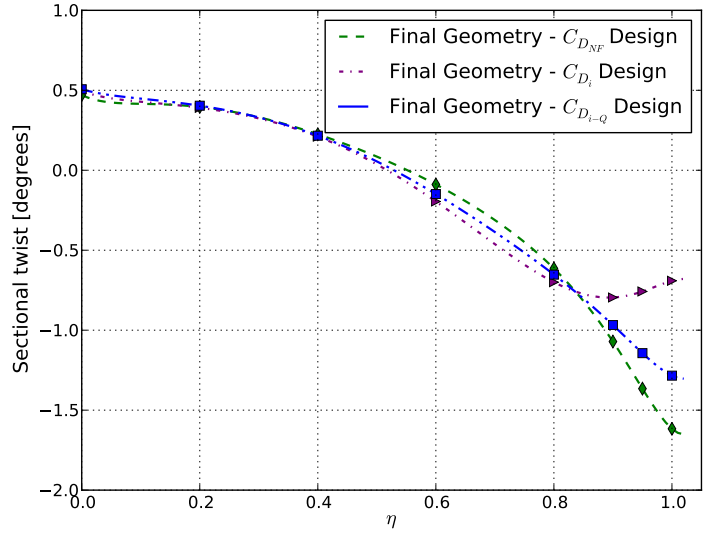

(b) Twist Distribution

Figure 5–23: Twist Optimization for NACA 0012-*modified* Wing at $M = 0.50$ and $C_L = 0.375$ - Supercoarse Grid (Part II)

induced drag with the novel *Q-criterion* based correction ($C_{D_{i-Q}}$) or the near-field drag ($C_{D_{NF}}$) has a reduced mesh dependency as the final design produced on the supercoarse grid better approaches that obtained on the coarse grid. It appears that the strong tip vortex produced on the simple rectangular grid hereby studied may have a large influence on the optimization process, most particularly for C_{D_i} driven optimization. A broader range of geometries, where some may produce weaker tip vortices (such as winglets, and/or tapered wings), will have to be studied to further conclude on the relative mesh dependency of each approach for induced drag minimization.

5.4 Transonic Optimization of the NACA 0012 Wing in Inviscid Flow

As Section 5.2.3 shows the ability of the proposed approach to minimize the induced drag without regard to the strength and location of a shock wave, this section investigates the ability of the proposed approach to minimize wave drag without regard to the induced drag. Again, the objective here is to look at the capability of the proposed approach to threat each phenomenological component of drag independently which can be particularly insightful for aircraft designers.

Shock mitigation using the proposed approach in inviscid lifting condition is studied in this section. The optimization problem is posed as,

$$\begin{aligned} \text{minimize} \quad & C_{D_{NF}} \text{ or } C_{D_w} \\ \text{subject to:} \quad & |C_L - C_{L_{\alpha=3.5^o}}| \leq 0.001, \end{aligned}$$

where $C_{D_{NF}}$, C_{D_w}, and C_L are the near-field drag, wave drag, and the lift coefficients respectively. The Mach number is fixed at 0.70 and the angle-of-attack is set to 3.5^o

corresponding to the conditions shown in Figure 4–13(b) of Chapter 4. The coarse grid described in Section 4–1 is employed.

5.4.1 Parametrization

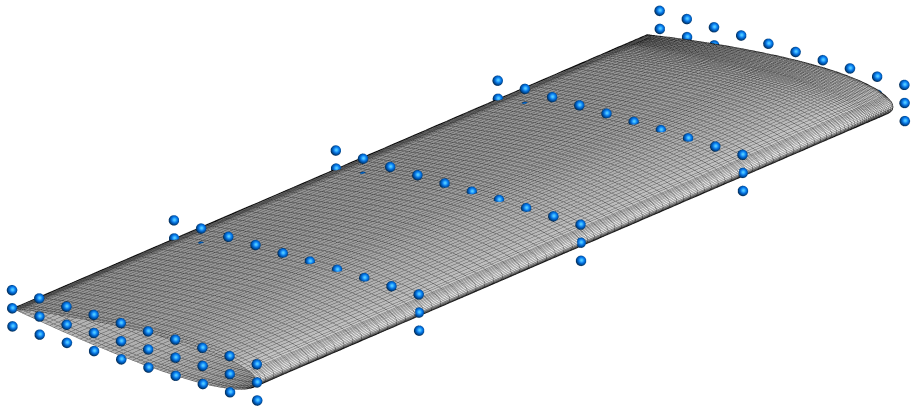

Figure 5–24: NACA0012-*modified* Wing with FFD parametrization - lattice box with $10 \times 3 \times 5$ control points (blue) shown.

A free-form deformation (FFD) approach using trivariate Bernstein polynomial [38] is used to parametrize the wing deformation. Figure 5–24 shows the FFD lattice box with a total of 150 control points employed for the optimizations. The leading, trailing edges along with the wing root, and tip are kept stationary by fixing the FFD control points at the edges, while the vertical displacement of the 72 interior control points served as design variables.

Table 5–5: NACA 0012-*modified* Wing at $M = 0.70$ and $\alpha = 3.5^o$ - Optimization results (drag values shown in counts)

	C_L	$C_{D_{NF}}$	$C_{D_{i-Q}}$	C_{D_w}
Initial geometry	0.359	89.4	70.0	13.7
$C_{D_{NF}}$ Design - Constrained Opt.	0.358	77.7	68.8	1.3
C_{D_w} Design - Constrained Opt.	0.359	80.9	69.5	2.1

5.4.2 Results

Figure 5–25 shows the optimality condition and C_L versus major iteration steps for the two optimization cases. The optimality condition is shown to drop by approximately an order of magnitude for both objective functions, and the lift is maintained between predetermined bounds.

The evolutions of $C_{D_{NF}}$, C_{D_w}, $C_{D_{i-Q}}$, and e w.r.t. $C_{D_{i-Q}}$ through the major iteration steps are depicted on Figure 5–25. The green curves denote optimization driven by the near-field drag while the purple curves demonstrate the optimization driven by the wave drag. The initial and final lift distributions are also depicted on the same figure. The final lift and drag coefficients are shown in Table 5–5. All optimization cases are able to reduce the wave drag from 13.7 to ~ 2 drag counts or below.

Figure 5–27 shows the pressure coefficients and wing cross-sections at various spanwise stations for the initial and optimized geometries. The optimizations for $C_{D_{NF}}$ and C_{D_w} failed to remove the shocks completely, but achieved final wave drag counts of 1.3 and 2.1, respectively. The same problem will be studied using additional FFD control points and/or a different parametrization method to assess if the inability to mitigate the shock entirely is associated to the parametrization employed.

The wave drag approach reduces the wave drag by more than 10 drag counts while very slightly altering the induced drag (< 0.2 count). Furthermore, the wave drag approach does not significantly modify the lift distribution. The near-field approach on the other hand successfully reduces the wave drag, but also significantly reduces the induced drag by altering the lift distribution. The ability of the proposed approach to minimize wave drag without regard to induced drag in an inviscid transonic lifting condition is thus observed: the near-field approach does not have this capability.

.

5.5 Wave Drag Minimization of CRM Wing in Viscous Conditions

Finally, shock mitigation in viscous flow is studied over the CRM wing geometry in this section. The optimization problem is posed as,

$$\begin{aligned} \text{minimize} \quad & C_{D_{p-NF}} \\ \text{subject to:} \quad & |C_L - 0.500| \leq 0.0005 \\ & C_M \geq -0.17 \\ & V_{Final} \geq V_{initial}, \end{aligned}$$

where $C_{D_{p-NF}}$ denotes the near-field pressure drag, C_M the pitching moment, and V the interior volume of the wing. The Mach number is fixed at 0.85 corresponding to the conditions shown in Section 4.3. This optimization problem represents the most complex case investigated as part of this thesis and the most representative of an actual aircraft wing design. While only the near-field pressure drag is used as the

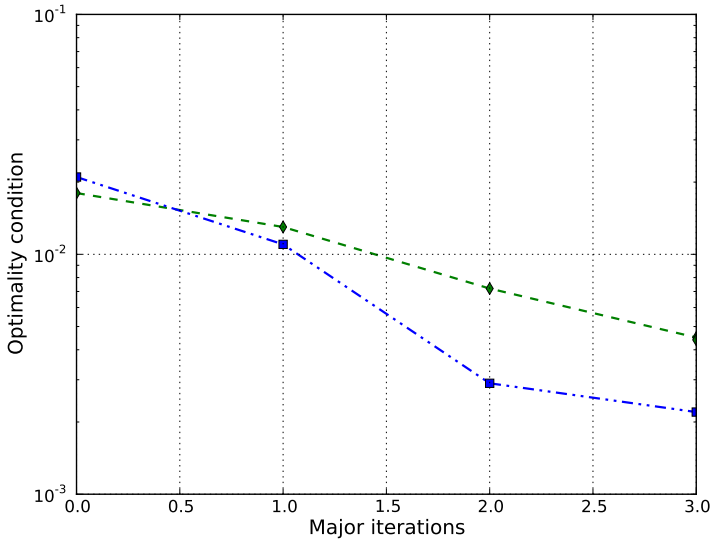

(a) Optimality

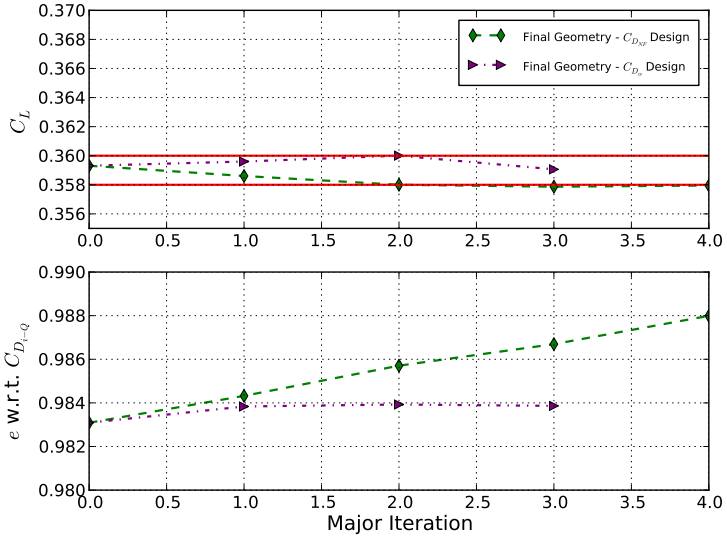

(b) C_L and Span Efficiency

Figure 5–25: Constrained Optimization for NACA 0012-*modified* Wing at $M = 0.70$ and $\alpha = 3.5^o$ - Coarse Grid (Part I)

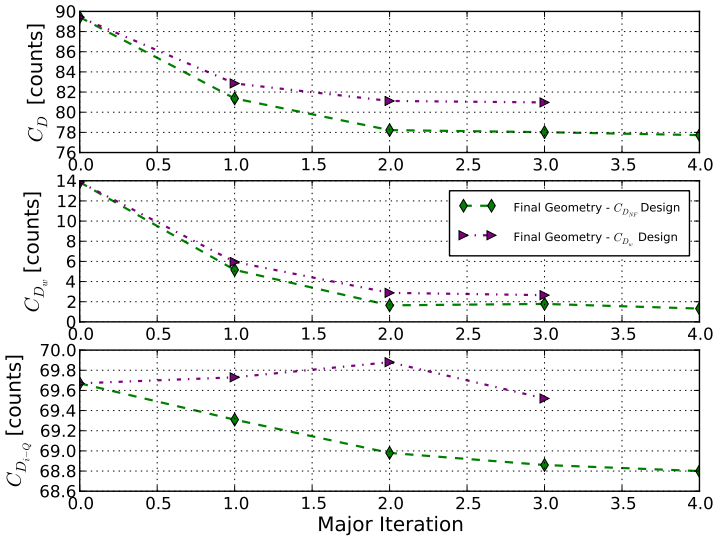

(a) $C_{D_{NF}}$, C_{D_w} and $C_{D_{i-Q}}$

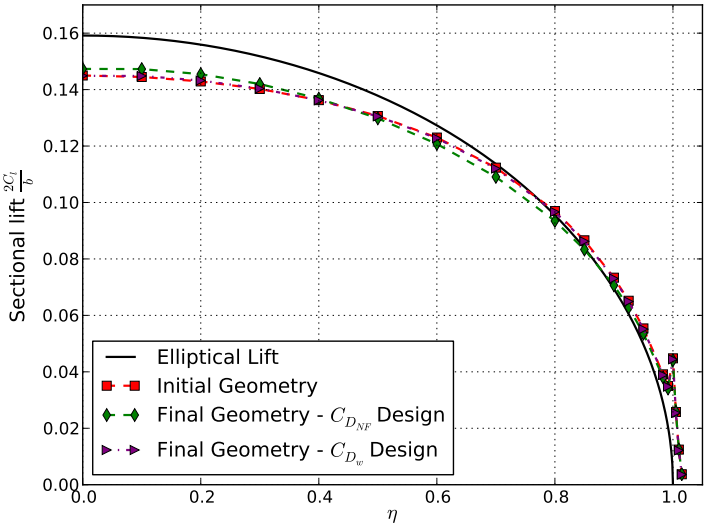

(b) Lift Distribution

Figure 5–26: Constrained Optimization for NACA 0012-*modified* Wing at $M = 0.70$ and $\alpha = 3.5^o$ - Coarse Grid (Part II)

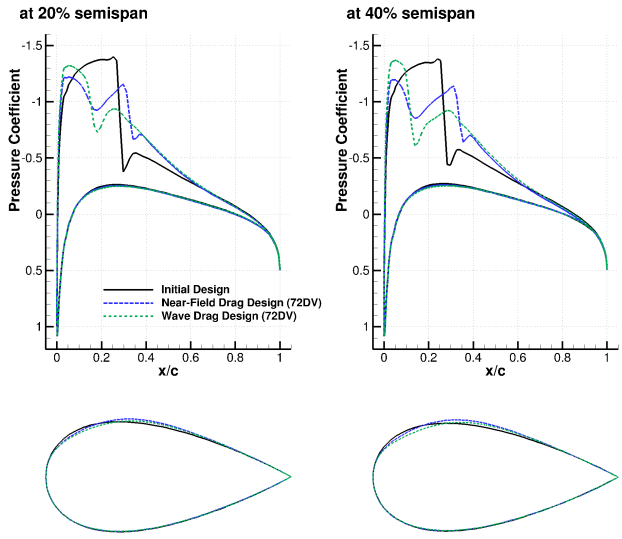

(a) Inboard span locations

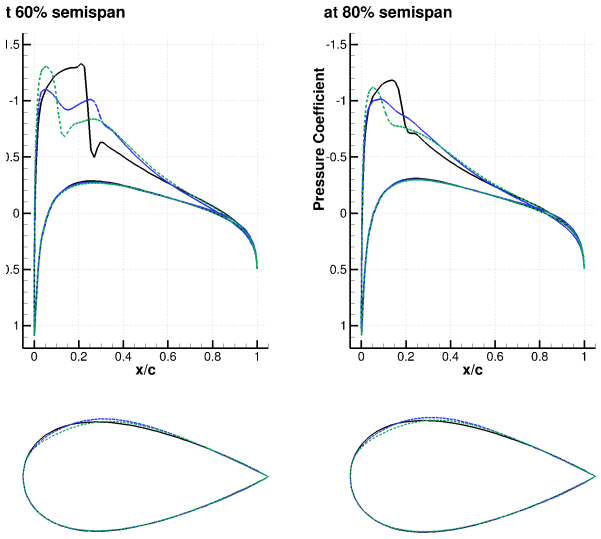

(b) Outboard span locations

Figure 5–27: Pressure coefficients for optimizations NACA 0012-*modified* Wing at $M = 0.70$ and $\alpha = 3.5^o$ - Coarse grid

objective function - i.e. no far-field drag components are used - the present case is shown as a possible future application of the approach presented in this thesis.

5.5.1 Parameterization

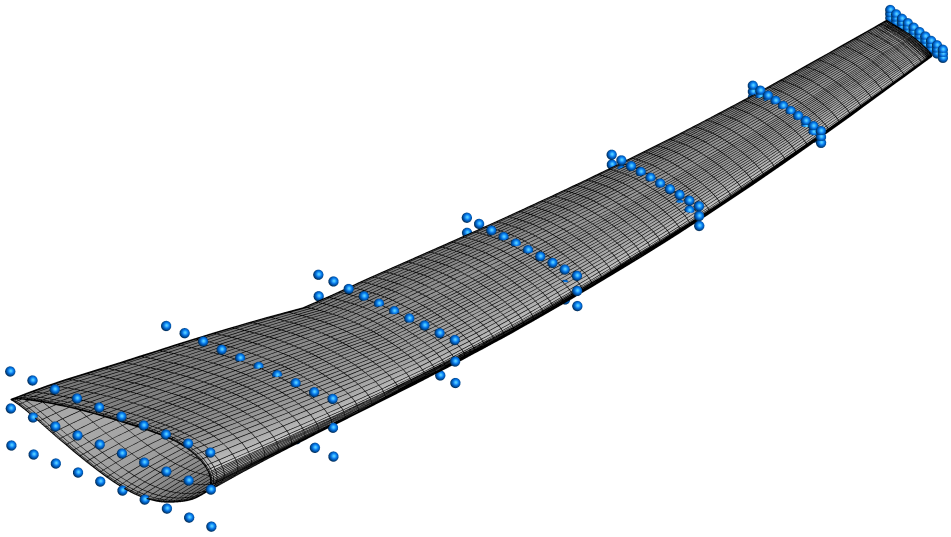

Figure 5–28: Baseline CRM Wing Geometry and FFD parametrization - lattice box with $10 \times 3 \times 5$ control points (blue) shown.

The vertical displacement of FFD control points are used as the design variable. The lattice box of the FFD parametrization has been analytically mapped to fit the CRM wing contour as depicted on Figure 5–28. As for the transonic optimization of the NACA 0012 wing shown in the previous section, the control points at the outer edges for the FFD lattice box has been fixed to limit the displacement at the wing root, and tip and at the leading and trailing edges. The results presented are based on the FFD parameterization with a total of 168 design variables stationed at 7 spanwise locations.

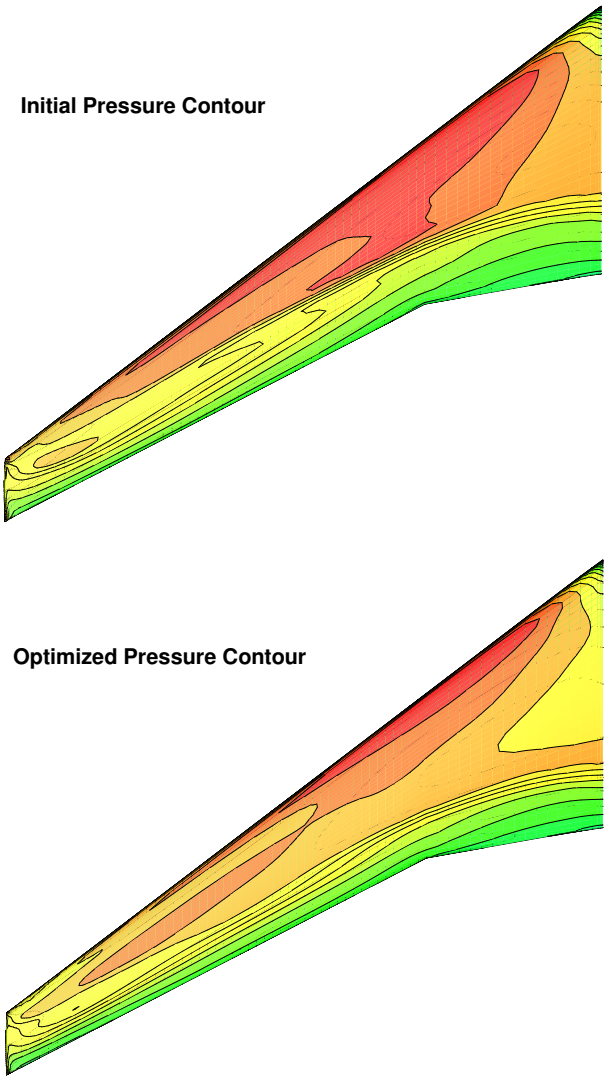

Figure 5–29: CRM Wing at $M = 0.85$ and $C_L = 0.500$ - Pressure Contour of Initial and Final Design

5.5.2 Results

Figure 5–29 depicts the initial and final pressure contours. The primary shock strength is severely weakened if not eliminated for much of the span locations. The spanwise pressure coefficient distributions is shown in Figure 5–31, where this is

further illustrated. The shock wave at the wing root is weakened but not removed. At all span stations, the pressure distribution in the lower surface is adjusted to ensure that the lift coefficient is within the constraint limits. Figure 5–32 depicts the changes to the airfoil surface at the same six specified spanwise stations. The volume constraint is satisfied through an increase in the rearward chord-wise thickness to compensate for the reduction in the forward region to decelerate the flow to reduce the drag coefficients. Volume was maintained at 0.01%, while the bounds on both lift and the pitching moment constraints were set at 0.5%.

Figures 5–30(a) through 5–30(c) demonstrate the evolution of the aerodynamic performance values as a function of the function values.

For the first 44 function calls the drag coefficient reduced by 4 counts from the initial 218.9 counts, while the lift and the pitching moment constraints were held within the bounds. The skin friction coefficient increased by half a count. A further reduction to 211.5 counts was achieved after 56 function calls. The lift coefficient at this stage was violated to 0.8%; while the pitching moment constraint moved to the upper bound. Reasons for the violation will be further investigated as part of future work. The optimality condition reduced by only an order of magnitude after the 56 function calls.

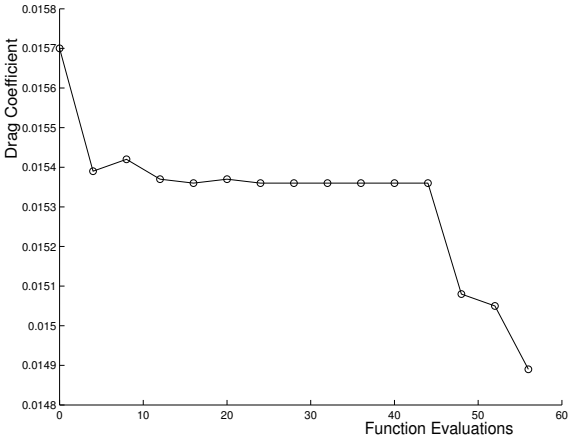

(a) Convergence of $C_{D_{p-NF}}$

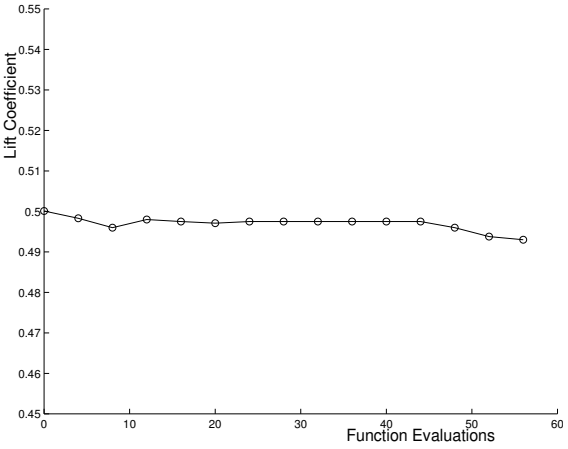

(b) Lift Constraint

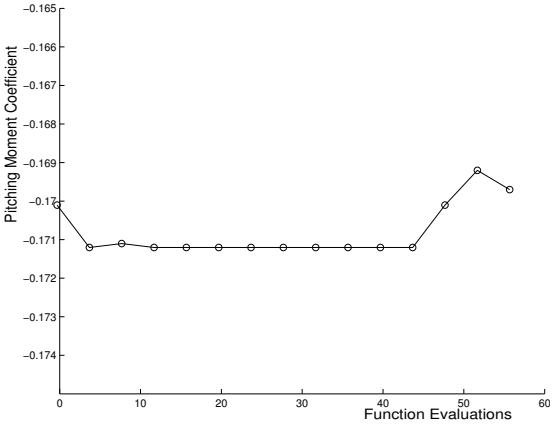

(c) Pitching Moment Constraint

Figure 5–30: CRM Wing at $M = 0.85$ and $C_L = 0.500$ - Optimization results

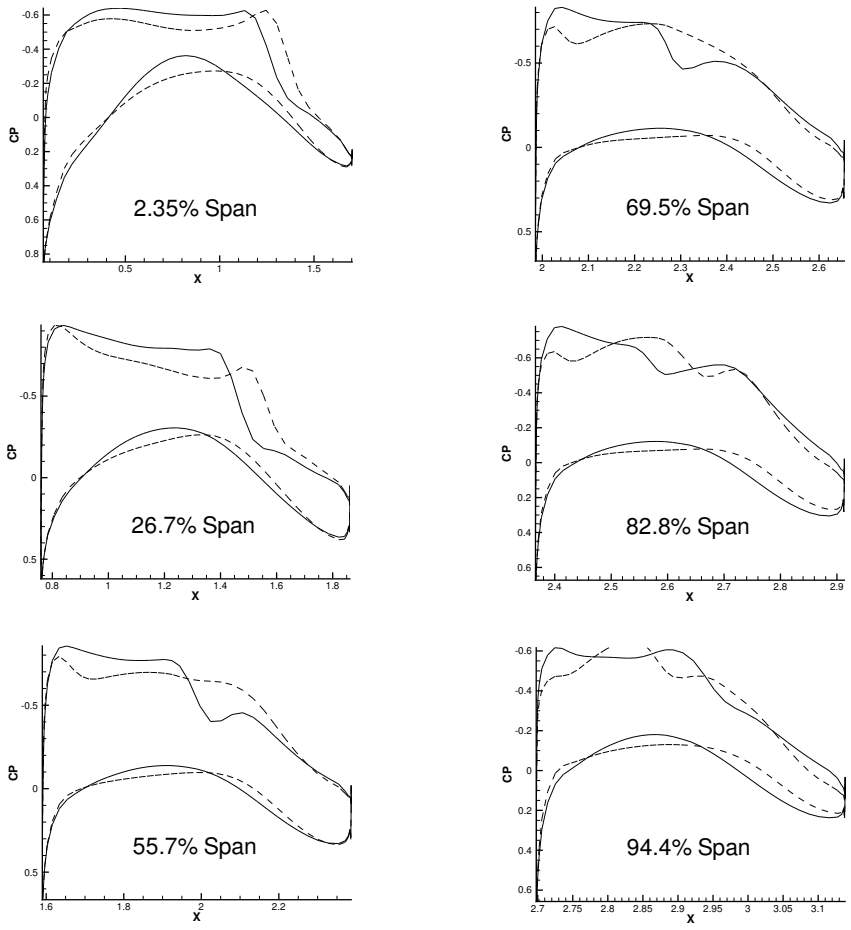

Figure 5–31: CRM Wing at $M = 0.85$ and $C_L = 0.500$ - Coefficient of pressure of initial and final designs at specified spanwise locations

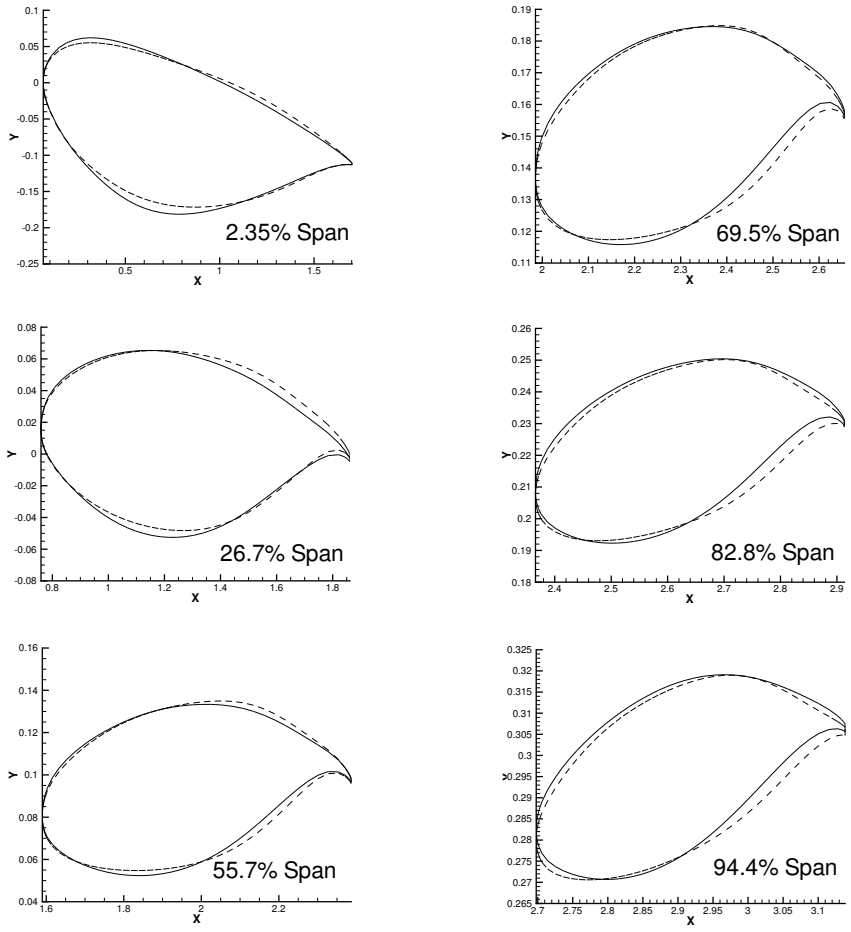

Figure 5–32: CRM Wing at $M = 0.85$ and $C_L = 0.500$ - Section airfoil geometry of initial and final designs at specified spanwise locations

CHAPTER 6
Conclusions

The motivation behind this work is to provide an efficient and robust numerical optimization tool to assist designers to increase the aerodynamic performance of aircraft and improve their understanding of the design space. The novel contributions of this work are the linearization and implementation of the adjoint-based gradient of the far-field drag components in an efficient optimization framework along with a novel *Q-criterion* based correction to induced drag.

Various drag decomposition methods and their implementation in a numerical flow solver are validated on several geometries and conditions ranging from inviscid subsonic flow to viscous transonic flow. The far-field methods are shown effective and less mesh dependent than the near-field method. Induced drag calculations using the *Q-criterion* based correction is shown to be more accurate than the uncorrected induced drag formulations, most particularly at coarser grid levels.

Adjoint-based aerodynamic shape optimizations based on the far-field drag components are presented and shown effective for increasingly complex cases. When applied for induced drag minimization, the proposed approach yielded span efficiency improvements of up to 3.0% on the DPW-W1 wing and the NACA 0012 rectangular wing. Wave drag minimization produced drag reduction of up to 16 drag counts, comparable to the more traditional near-field approach, on NACA 0012 based wings. Adjoint-based optimization using the novel *Q-criterion* based correction to induced

drag was shown to be less mesh dependent than the near-field drag, then other more traditional formulations of far-field induced drag.

Furthermore, the ability of the proposed approach to threat each phenomenological components of drag independently is highlighted on two constrained optimization cases in transonic lifting conditions. While the near-field may be sufficient for the design of an aircraft wing, the ability of the drag decomposition approach to determine how the various aspects of the wing contribute towards the total drag coefficient may be insightful for designers. The proposed framework may potentially allow assigning design variables best suited for each phenomenological component of drag, thus potentially providing a more efficient design tool.

6.1 Future Work

Several opportunities to extend and/or refine the aerodynamic optimization framework presented in this work are identified, namely:

1. **Linearization of shock and viscous sensors**. Derive a complete linearization of the wave and viscous drag components. This will increase the accuracy of the adjoint-based gradients.
2. **Application of the framework to viscous simulations**. Extend the viscous optimization presented in this thesis to drag minimization employing the far-field drag components. Investigate the dependency of the optimization on mesh size and quality in viscous flows.
3. **Application of the framework for various geometries and associated parameterization**. Apply the drag decomposition approach for more complex industrial cases to further demonstrate the capabilities of the proposed

approach. A possible application is to the design of winglets, and to the optimization of the CRM wing-fuselage configuration.

4. **Mesh adaptation based on decomposed drag components**. The adjoint-based sensitivities could be used as part of a mesh adaptation scheme, and coupled with the optimization framework could lead to more robust designs.

References

[1] AIAA. Aerodynamic design optimization discussion group. https://info.aiaa.org/tac/ASG/APATC/AeroDesignOpt-DG/default.aspx, 2015-01-20.

[2] AIAA. Fifth drag prediction workshop. http://aaac.larc.nasa.gov/tsab/cfdlarc/aiaa-dpw/Workshop5/workshop5.html, 2015-01-20.

[3] AIAA. Fourth drag prediction workshop. http://aaac.larc.nasa.gov/tsab/cfdlarc/aiaa-dpw/Workshop4/workshop4.html, 2015-01-20.

[4] AIAA. Third drag prediction workshop. http://aaac.larc.nasa.gov/tsab/cfdlarc/aiaa-dpw/Workshop3/workshop3.html, 2015-01-20.

[5] AIAA. Sixth drag prediction workshop. http://aaac.larc.nasa.gov/tsab/cfdlarc/aiaa-dpw/, 2015-07-31.

[6] B. S. Baldwin and H. Lomax. Thin layer approximation and algebraic model for separated flows. In *AIAA 16th Aerospace Sciences Meeting*, Huntsville, 1978. AIAA Paper 1978-257.

[7] F. Bisson and S. Nadarajah. Adjoint-based shape optimization for induced drag. In *32nd AIAA Applied Aerodynamics Conference - AIAA Aviation 2014*, Atlanta, 2014. AIAA Paper 2014-3176.

[8] F. Bisson and S. Nadarajah. Adjoint-based aerodynamic optimization of benchmark problems. In *53rd Aerospace Sciences Meeting - AIAA SciTech 2015*, Kissimmee, 2015. AIAA Paper 2015-1948.

[9] F. Bisson and S. Nadarajah. Adjoint-based aerodynamic design optimization using the drag decomposition method. In *31st AIAA Applied Aerodynamics Conference*, San Diego, 2013. AIAA Paper 2013-2909.

[10] F. Bisson, S. Nadarajah, and D. Shi-Dong. Adjoint-based aerodynamic optimization of benchmark problems. In *52nd Aerospace Sciences Meeting - AIAA SciTech 2014*, National Harbor, 2014. AIAA Paper 2015-1948.

[11] M.D. Buhmann. *Radial basis functions*, volume 12 of Cambridge monographs on applied and computational mathematics. Cambridge University Press, New York, 2003.

[12] G. Carrier, D. Destarac, A. Dumont, M. Meheut, I. Salah El Din, J. Peter, S. Ben Khelil, J. Brezillon, and M. Pestana. Gradient-based aerodynamic optimization with the elsA software. In *52nd Aerospace Sciences Meeting - AIAA SciTech 2014*, National Harbor, 2014. AIAA Paper 2014-0568.

[13] D. D. Chao and C. P. van Dam. Wind drag prediction and decomposition. *Journal of Aircraft*, 43(1):82–90, 2006.

[14] A. de Boer, M.S. van der Schoot, and H. Bijl. Mesh deformation based on radial basis function interpolation. *Computers and Structures*, 85:784–795, 2007.

[15] D. Destarac and J. van der Vooren. Drag/thrust analysis of jet-propelled transonic transport aircraft; definition of physical drag components. *Aerospace Science and Technology*, 8(6):545–556, 9 2004.

[16] M. B. Giles and R. M. Cummings. Wake integration for three-dimensional flowfield computations: Theoretical development. *Journal of Aircraft*, 36(2):357–365, 1999.

[17] P. E Gill, W. Murray, and M. A Saunders. SNOPT: An SQP algorithm for large-scale constrained optimization. *SIAM review*, 47(1):99–131, 2005.

[18] P. E. Gill, W. Murray, and M. A. Saunders. *Users Guide for SNOPT Version 7: Software for Large-Scale Nonlinear Programming*, 2008. Manual.

[19] G. Haller. An objective definition of a vortex. *Journal of Fluid Mechanics*, 525:1 – 26, 2005.

[20] J. E. Hicken and D. W. Zingg. Induced-drag minimization of nonplanar geometries based on the euler equations. *AIAA Journal*, 48(11):2564–2575, 2010.

[21] D. Hue and S. Esquieu. Computational drag prediction of the DPW4 configuration using the far-field approach. *Journal of Aircraft*, 48(5):1658–1670, 2011.

[22] D. L. Hunt, R. M. Cummings, and M. B. Giles. Wake integration for three-dimensional flowfield computations: Applications. *Journal of Aircraft*, 36(2):366–373, 1999.

[23] ANSYS Inc. ICEM CFD software webpage. `http://www.ansys.com/Products/Other+Products/ANSYS+ICEM+CFD`, 2015-07-02.

[24] A. Jameson. A non-oscillatory shock capturing scheme using flux limited dissipation. MAE Report 1653, Princeton University, Princeton, New Jersey, April 1984. Published in *Lectures in Applied Mathematics*, B.E. Engquist, S. Osher, and R.C.J. Sommerville, editor, A.M.S., Part 1, 22:345–370, 1985.

[25] A. Jameson. Aerodynamic design via control theory. *Journal of Scientific Computing*, 3(3):233–260, 1988.

[26] A. Jameson, W. Schmidt, and E. Turkel. Numerical solutions of the euler equations by finite volume methods with runge-kutta time stepping schemes. In *AIAA 14th Fluid and Plasma Dynamics Conference*, Palo Alto, CA, 1981. AIAA Paper 81-1259.

[27] G. K.W. Kenway, G. J. Kennedy, and J. R. R. A. Martins. A CAD-free approach to high-fidelity aerostructural optimization. In *13th AIAA/ISSMO Multidisciplinary Analysis Optimization Conference*, Forth Worth, 2010. AIAA Paper 2010-9231.

[28] K. Kusunose and J. P. Crowder. Extension of wake-survey analysis method to cover compressible flows. *Journal of Aircraft*, 39(6):954 – 963, 2002.

[29] D. Levy, K. Laflin, E. Tinoco, J. Vassberg, B. Rider, M. Mani, C. Rumsey, R. Wahls, J. Morrison, O. Brodersen, S. Crippa, D. Mavriplis, and M. Murayama. Summary of data from the fifth AIAA CFD drag prediction workshop. In *51st AIAA Aerospace Sciences Meeting including the New Horizons Forum and Aerospace Exposition*, Dallas, 2013. AIAA Paper 2013-46.

[30] W. E. Lorensen and H. E. Cline. Marching cubes: A high resolution 3D surface construction algorithm. *Computer Graphics*, 21(4):163–169, 1987.

[31] D. Lovely and R. Haimes. Shock detection from computational fluid dynamics results. In *14th AIAA Computional Fluid Dynamics Conference*, Norfolk, 1999. AIAA Paper 1999-3285.

[32] G. K. Lyu, Z. Kenway and J. R. R. A. Martins. RANS-based aerodynamic shape optimization investigations of the common research model wing. In *52nd Aerospace Sciences Meeting - AIAA SciTech 2014*, National Harbor, 2014. AIAA Paper 2014-0567.

[33] E. C. Maskell. Progress towards a method for the measurement of the components of the drag of a wing of finite span. Royal Aircraft-Establishment, RAE TR 72232, London, 1972.

[34] F. Menter. Two-equation eddy-viscosity turbulence models for engineering applications. *AIAA Journal*, 32(8):1598–1605, August 1994.

[35] S. Nadarajah. *The Discrete Adjoint Approach to Aerodynamic Shape Optimization*. PhD thesis, Stanford University, Dept. of Aeronautics and Astronautics, 2003.

[36] S. A. Ning and I. Kroo. Multidisciplinary considerations in the design of wings and wing tip devices. *Journal of Aircraft*, 47(2):534–543, 2010.

[37] L. Paparone and R. Tognaccini. Computational fluid dynamics-based drag prediction and decomposition. *AIAA Journal*, 41(9):1647 – 57, 2003.

[38] L. Piegl and W. Tiller. *The NURBS Book*. Springer, New York, 2nd edition edition, 1997.

[39] O. Pironneau. Optimal shape design for elliptic systems. In *System Modeling and Optimization*, volume 38 of *Lecture Notes in Control and Information Sciences*, pages 42–66. Springer Berlin Heidelberg, 1982.

[40] V. Poirier. An efficient radial basis function mesh deformation scheme within an adjoint-based aerodynamic optimization framework. Master's thesis, McGill University, Montreal, Quebec, August 2011.

[41] M. Ueno, K. Yamamoto, K. Tanaka, M. Murayama, and R. Tognaccin. Far-field drag analysis of nasa common research model simulation. *Journal of Aircraft*, 50:388–397, 2013.

[42] B. Walther. *Adjoint-based constrained aerodynamic shape optimization for multistage turbomachines*. PhD thesis, McGill University, Dept. of Mechanical Engineering, 2014.

[43] H. Wendland. *Scattered data approximation*, volume 17 of Cambridge monographs on applied and computational mathematics. Cambridge University Press, New York, 2005.

[44] W. Yamazaki, K. Matsushima, and K. Nakahashi. Drag prediction and decomposition based on CFD computations. *JSME International Journal, Series B (Fluids and Thermal Engineering)*, 48(2):235 – 40, 2005.

[45] W. Yamazaki, K. Matsushima, and K. Nakahashi. Aerodynamic design optimization using the drag-decomposition method. *AIAA Journal*, 46(5):1096, May 2008.

[46] W. Yamazaki, K. Matsushima, and K. Nakahashi. Application of drag decomposition method to CFD computational results. In *23rd AIAA Applied Aerodynamics Conference*, Toronto, 2005. AIAA Paper 2005-4723.